frontiers | Frontiers in Materials

TYPE Original Research
PUBLISHED 03 October 2024
DOI 10.3389/fmats.2024.1466793



OPEN ACCESS

EDITED BY
Alireza Tabarraei,
University of North Carolina at Charlotte, United States

REVIEWED BY
Xingyu Gao,
Institute of Applied Physics and Computational Mathematics (IAPCM), China
Prashant Singh,
Iowa State University, United States

*CORRESPONDENCE
Anju Chandran,
anju.chandran@hereon.de

RECEIVED 18 July 2024
ACCEPTED 20 September 2024
PUBLISHED 03 October 2024

CITATION
Chandran A, Santhosh A, Pistidda C, Jerabek P, Aydin RC and Cyron CJ (2024) Comparative analysis of ternary TiAlNb interatomic potentials: moment tensor vs. deep learning approaches.
*Front. Mater.* 11:1466793.
doi: 10.3389/fmats.2024.1466793



# Comparative analysis of ternary TiAlNb interatomic potentials: moment tensor vs. deep learning approaches

Anju Chandran[1]*, Archa Santhosh[2], Claudio Pistidda[2], Paul Jerabek[2], Roland C. Aydin[1,3] and Christian J. Cyron[1,3]

[1]Institute of Material Systems Modeling, Helmholtz-Zentrum Hereon, Geesthacht, Germany, [2]Institute of Hydrogen Technology, Helmholtz-Zentrum Hereon, Geesthacht, Germany, [3]Institute for Continuum and Material Mechanics, Hamburg University of Technology, Hamburg, Germany

Intermetallic titanium aluminides, leveraging the ordered $\gamma$-TiAl phase, attract increasing attention in aerospace and automotive engineering due to their favorable mechanical properties at high temperatures. Of particular interest are $\gamma$-TiAl-based alloys with a Niobium (Nb) concentration of 5–10 at.%. It is a key question how to model such ternary alloys at the atomic scale with molecular dynamics (MD) simulations to better understand (and subsequently optimize) the alloys. Here, we present a comparative analysis of ternary TiAlNb interatomic potentials developed by the moment tensor potential (MTP) and deep potential molecular dynamics (DeePMD) methods specifically for the above mentioned critical Nb concentration range. We introduce a novel dataset (TiAlNb dataset) for potential training that establishes a benchmark for the assessment of TiAlNb potentials. The potentials were evaluated through rigorous error analysis and performance metrics, alongside calculations of material properties such as elastic constants, equilibrium volume, and lattice constant. Additionally, we explore finite temperature properties including specific heat and thermal expansion with both potentials. Mechanical behaviors, such as uniaxial tension and the calculation of generalized stacking fault energy, are analyzed to determine the impact of Nb alloying in TiAl-based alloys. Our results indicate that Nb alloying generally enhances the ductility of TiAl-based alloys at the expense of reduced strength, with the notable exception of simulations using DeePMD for the $\gamma$-TiAl phase, where this trend does not apply.

KEYWORDS

**TiAlNb alloy, machine-learning interatomic potentials, deep learning, moment tensor, molecular dynamics, density functional theory**

## 1 Introduction

Gamma titanium aluminide ($\gamma$-TiAl) intermetallic alloys attract increasing attention in aerospace and automotive engineering as high-performance lightweight structural materials. This growing interest is primarily due to their unique combination of low density, remarkable oxidation resistance, and superior strength and creep resistance at elevated temperatures Appel et al. (2011). Key to these alloys are the primary intermetallic phases: $\gamma$-TiAl, with its ordered face-centered tetragonal structure ($L1_0$, P4/mmm) and $\alpha_2$-$Ti_3Al$, noted for its ordered hexagonal structure ($D0_{19}$, $P6_3/mmc$). The advancement of

$\gamma$-TiAl based alloys, particularly those tailored for higher service temperatures, such as TNM (TiAl-Nb-Mo) and TNB (TiAl-Nb-B) alloys, has been significant (Appel et al., 2011; Clemens and Mayer, 2012; Li et al., 2014; Klein et al., 2016; Zhang et al., 2016). These alloys typically contain 5–10 at.% Nb, along with small amounts of other elements like Mo, B, C, Si, W, Cr, Ta. Extensive research highlights Nb's crucial role in boosting mechanical properties, notably increasing the strength and ductility of TiAl alloys (Appel et al., 2011; Clemens and Mayer, 2012; Liu et al., 2002; Song et al., 2020; Cheng et al., 2016; Liu et al., 2022; Zhang et al., 2023). Despite these improvements, the specific contribution of Nb to the enhancement of strength and ductility in TNB and TNM alloys has remained somewhat unclear. In our previous work (Chandran et al., 2024), we addressed this gap by examining the effects of Nb on the thermo-mechanical properties of TiAl-based alloys through atomistic simulations. Utilizing Farkas' ternary interatomic potential (Farkas and Jones, 1996), we scrutinized various TiAl-based models, ranging from single-phase structures to single lamellar interfaces, and progressing to more complex microstructure-informed atomistic models (MIAMs) with nano-polycolonies. However, it became evident that it is a limitation of Farkas' potential that it could not adequately handle Nb concentrations above 1 at.% in MIAMs and 2 at.% in certain types of single lamellar interfaces. This limitation is significant, as higher Nb concentrations (5–10 at.%) are known to be most interesting for improving strength and ductility. To overcome this challenge, we pursue in this article the direction of developing machine learning (ML) -based interatomic potentials for molecular dynamics (MD) simulations.

Generally, MD simulations offer profound insights into the behavior of atomic systems, ranging in scale from around $10^3$–$10^9$ atoms. These simulations are instrumental in capturing a wide array of interactions, including thermal, mechanical, chemical, and microstructural dynamics. However, the accuracy of MD simulations is contingent upon the selection of appropriate interatomic potentials or force fields, as well as the boundary conditions implemented. In recent years, the integration of machine learning with MD simulations has emerged as a rapidly evolving field. This integration primarily focuses on the modeling of interatomic potential energy surfaces (PES) using reference data derived from *ab initio* simulations. Various ML methodologies have made significant contributions to the study of condensed matter systems and can be broadly categorized into linear regression [e.g., moment tensor potentials (Shapeev, 2016; Podryabinkin and Shapeev, 2017; Gubaev et al., 2019)], kernel methods [e.g., gaussian approximation potential (Bartók et al., 2013; Szlachta et al., 2014; Dragoni et al., 2018), spectral neighbor analysis (Thompson et al., 2015; Chen et al., 2017; Li et al., 2018; Deng et al., 2019)], and deep neural network-based techniques (Behler and Parrinello, 2007; Behler, 2011; Zhang et al., 2018a), respectively.

Recent comparative studies have evaluated the effectiveness of these diverse techniques, as seen in the works of Zuo et al. (2020); Deringer et al. (2019); Unke et al. (2020, 2021). Among these, deep neural network-based potentials, particularly the deep potential (DP) and neural network potential (NNP), stand out due to their successes in modeling both ordered and disordered systems. The flexibility of the descriptor proposed by Zhang et al. (2018a) for DP potentials is particularly noteworthy. The DP method has demonstrated its efficacy in various systems, such as LiF and FLiBe (Rodriguez et al., 2021), $MgCl_2$-NaCl and $MgCl_2$-KCl (Xu et al., 2023), AlN (Li et al., 2024), Cu (Du et al., 2022) and several others (Niu et al., 2020; Nguyen et al., 2022). In comparison, the moment tensor potential (MTP) is notable for its efficiency, derived from a polynomial basis of interatomic distances and angles. MTP not only outpaces the other methods in terms of speed but has also demonstrated equivalent accuracy in modeling various material systems, as shown in studies by Novikov et al. (2018); Podryabinkin et al. (2019); Novoselov et al. (2019). MTP has been recognized for its optimal balance between accuracy and computational efficiency, a comparison elucidated in Zuo et al. (2020) performance analysis. Tasnádi et al. (2021) developed an MTP potential for efficiently predicting the elastic properties of $Ti_{0.5}Al_{0.5}N$. Furthermore, the work by Lu et al. (2023) deserves attention, where the authors generated a DeePMD potential for TiAlNb. They assert that this potential successfully validates the bulk material properties of TiAl-based alloys and provides accurate evaluations of the stacking fault energy and tensile properties of $\gamma$-TiAl. It is also worth mentioning that the neuroevolution potential (NEP) method, as used in the study by Zhao et al. (2024), was applied to train a general-purpose Ti-Al-Nb potential. The authors claim that this trained potential not only explains the high-temperature mechanical properties of TiAl-based alloys but also accurately reproduces the fundamental material properties.

In this paper, we initially create essential datasets for training TiAlNb-based interatomic potentials using *ab initio* molecular dynamics (AIMD) simulations. These datasets (TiAlNb datasets) are intended to serve as a benchmark for evaluating TiAlNb-based interatomic potentials. Utilizing them, we train the TiAlNb interatomic potentials using both MTP and DP methods. Subsequently, we conduct a comparative evaluation of these potentials through error analysis and performance metrics, in addition to calculating material properties such as elastic constants, equilibrium volume, and lattice constants. We further compute finite temperature properties, including specific heat capacity and thermal expansion. Furthermore, we assess the mechanical properties by performing simulated uniaxial tension tests and calculations of generalized stacking fault energy.

# 2 Materials and methods

## 2.1 Dataset generation

We performed a large number of AIMD simulations with the Vienna *ab initio* simulation package (VASP) Kresse and Furthmüller (1996a); Kresse and Furthmüller (1996b). These simulations employed projector augmented wave (PAW) Blöchl, (1994) method to intricately model the interactions between electrons and ions. We incorporated the generalized gradient approximation (GGA) (Perdew et al., 1996, Perdew et al., 1997) for addressing exchange and correlation effects, specifically using the Perdew–Burke–Ernzerhof (PBE) functional. Our computational framework was rigorously set up with a significant cut-off energy of

510 eV, which was crucial for ensuring the accuracy and precision of our calculations. Furthermore, a Γ-centered k-point mesh of dimensions $1 \times 1 \times 1$ was employed to efficiently sample the Brillouin zone, striking a balance between computational efficiency and temporal resolution with a time step of 0.5 femtoseconds in all AIMD simulations.

For the development of the interatomic potential, we curated a comprehensive dataset encompassing a wide spectrum of Nb concentrations in $\gamma$-TiAl and $\alpha_2$-$Ti_3Al$ alloys, ranging from 1 at.% to 14 at.%. This compilation resulted in an extensive array of 28 unique structural configurations, featuring 108 atoms in $\gamma$-TiAl and 128 atoms in $\alpha_2$-$Ti_3Al$. Our primary focus was on the Nb concentration range of 1–10 at.%, although we extended our dataset to include concentrations up to 14 at.% Nb to enhance the training process. Among these 28 configurations, a subset was reserved and excluded from training to assess the potential's predictive accuracy. The introduction of Nb atoms into titanium lattice sites in both phases was carefully executed, taking into account the preferential site occupancy of Nb in these alloys. For a more detailed exposition of this methodology, readers are referred to our previous work (Chandran et al., 2024) and other pertinent literature (Holec et al., 2016; Ouadah et al., 2020; Ouadah et al., 2021; Song et al., 2000; Wei et al., 2012). The Atomsk tool (Hirel, 2015) was utilized for the precise generation of these datasets, ensuring an accurate representation of the structural configurations. It should be noted that defect configurations were not included in the training process.

Subsequent AIMD simulations were conducted with meticulous care across all these structures, using the NVT and NPT ensemble over a period of nearly 10 ps. To comprehensively analyze thermal behaviors, these simulations spanned a range of temperatures including 1 K, 300 K, 500 K, 700 K, and 900 K. In the NVT ensemble, particular attention was given to selecting frames post-equilibration for analysis. The snapshots derived from these AIMD simulations provided a rich and diverse data source for training both MTP and DeepMD potentials. The snapshots were partitioned in an 80:20 ratio between the training and test sets to optimize the learning process. More details of the training database are provided in the Supplementary Material, in Section 1.

The TiAlNb dataset developed for this research is now available for public access. It includes the initial structural files in VASP format, essential for generating AIMD frames, alongside the training and validation datasets for DeePMD, and the training and testing datasets for MTP. Additionally, input files necessary for model training are provided, ensuring that users can replicate the results. Access to the dataset is facilitated through the link: TiAlNb dataset offering comprehensive resources for further exploration and validation.

For training the DeePMD potential, we utilized the DeePMD kit (Wang et al., 2018) along with its corresponding library designed for integration with the LAMMPS package (Thompson et al., 2022) for executing MD simulations. Similarly, the training of the MTP potential was conducted using the MLIP package (Novikov et al., 2021), employing its library specifically developed for compatibility with the LAMMPS package (Thompson et al., 2022) to facilitate MD simulations.

## 2.2 MTP

MTP is a type of machine learning-developed interatomic potential, implemented using the MLIP package (Novikov et al., 2021). In MTP, the energy of each atomic configuration (denoted as $cfg$) is expressed as the sum of contributions from the local atomic neighborhoods $n_i$ for N atoms. This is mathematically represented as,

$$E^{mtp}(cfg) = \sum_{i=1}^{N} V(n_i), \tag{1}$$

where each contribution $V$ is linearly expanded via a set of basis functions $B_\alpha$,

$$V(n_i) = \sum_{\alpha=1}^{N_{lin}} \xi_\alpha B_\alpha(n_i). \tag{2}$$

In the above equation, the set of parameters $\xi = \{\xi_\alpha\}$ are derived during the training process and $N_{lin}$ is the number of these parameters. The atomic environments are characterized using moment tensor descriptors or moments, which include both radial and angular components. The moment tensor descriptor for the $i$-th atom is defined as,

$$M_{\mu,\nu}(n_i) = \sum_{j=1}^{N_{nbh}} f_\mu\left(|r_{ij}|, z_i, z_j\right) \underbrace{r_{ij} \otimes \cdots \otimes r_{ij}}_{\nu \text{ times}}, \tag{3}$$

where $r_{ij}$ is the position of $j$-th atom relative to $i$-th atom and $|r_{ij}|$ is the corresponding interatomic distance. $N_{nbh}$ is the number of atoms in neighborhood. The descriptor consists of the angular part, $\underbrace{r_{ij} \otimes \cdots \otimes r_{ij}}_{\nu \text{ times}}$ (the symbol '⊗' represents the outer product of vectors and, hence, the angular part is the tensor of order ν) and the radial part, $f_\mu(|r_{ij}|, z_i, z_j)$ having the following form,

$$f_\mu\left(|r_{ij}|, z_i, z_j\right) = \sum_{\beta=1}^{N_Q} c^{(\beta)}_{\mu,z_i,z_j} Q^{(\beta)}\left(|r_{ij}|\right), \tag{4}$$

where $\{c_{\mu,z_i,z_j}\}$ and $Q^{(\beta)}(|r_{ij}|)$ represents the set of radial parameters and radial basis functions, respectively.

The basis functions $B_\alpha$ are constructed using the *level* of moments:

$$levM_{\mu,\nu} = 2 + 4\mu + \nu, \tag{5}$$

These coefficients have been found to be optimal for many datasets Gubaev et al. (2019). The basis functions $B_\alpha$ are invariant to rotations, reflections, and permutations. For defining a functional form of MTP, we choose the maximum level, $lev_{max}$, and include all the basis functions whose level is less or equal to $lev_{max}$, i.e., $levB_\alpha \le lev_{max}$.

The MTP parameters $\theta$ comprise of the radial parameters $c$ and $\xi$, which are obtained during the fitting procedures. The fitting and learning procedure of MTP consists of finding parameters $\theta$ by minimizing the optimization problem,

$$\begin{aligned} \sum_{k=1}^{K} \Big[ & w_e \left(E^{mtp}(cfg_k;\theta) - E^{qm}(cfg_k)\right)^2 \\ & + w_f \sum_{i=1}^{N_k} \left| f_i^{mtp}(cfg_k;\theta) - f_i^{qm}(cfg_k) \right|^2 \\ & + w_s \left|\sigma^{mtp}(cfg_k;\theta) - \sigma^{qm}(cfg_k)\right|^2 \Big] \quad \rightarrow \min_\theta \end{aligned} \tag{6}$$

where the training set contains configurations $cfg_k, k = 1, \ldots, K$ and $E^{qm}(cfg_k)$, $f_i^{qm}(cfg_k)$ and $\sigma^{qm}(cfg_k)$ are the quantum mechanical energy, forces and stress tensors, respectively. $N_k$ is the number of atoms in configuration $k$ and $w_e$, $w_f$ and $w_s$ are the non-negative weights of energies, forces and stresses during the optimization. Equations 1–6 pertains to MTP formulation.

## 2.3 DeePMD

The DP method used in this study was developed using DeePMD kit (Wang et al., 2018). In DeePMD, the total energy of the system is represented as sum of energies of all the atoms. Suppose a system contains $N$ atoms, then the total energy of the system according to DeePMD model can be represented as,

$$E = \sum_{i=1}^{N} E_i. \tag{7}$$

Each atomic energy $E_i$ is obtained by the position of $i$-th atom and its neighbours,

$$E_i = E_{s(i)}\left(R_i, \left\{R_j | j \in N_{Rc}(i)\right\}\right), \tag{8}$$

where $s_i$ denotes the chemical specie of atom $i$ and $N_{Rc}(i)$ denotes the set of neighbour atoms that are at a cut-off radius of $R_c$ from atom $i$. The cut-off radius of the neighbouring atoms should be such that $R_{ij} = \mid R_i - R_j \mid \leq R_c$. In order to map the atomic positions, descriptors that guarantee translational, rotational and permutational symmetries are used. We have used the deep potential smooth edition (DeepPot-SE) Zhang et al. (2018b) suggested in DeePMD Kit that includes the radial and angular information of atomic configurations. These symmetry preserving descriptors are set up using an embedding net and are later passed to the fitting net to obtain the energy of each atom. Parameter optimization is performed by minimizing the loss function $L$ where,

$$L\left(p_\epsilon, p_f, p_\xi\right) = \frac{p_\epsilon}{N}|\Delta E^2| + \frac{p_f}{3N}\sum|\Delta F|^2 + \frac{p_\xi}{9N}\|\Delta\Xi\|^2, \tag{9}$$

where ΔE, ΔF and Δ Ξ correspond to the root mean square (RMS) error of energy, force and stress, respectively. During the optimization process, the prefactors of energy ($p_\epsilon$), force ($p_f$) and stress ($p_\epsilon$) are changed. The prefactors are formulated as

$$p(t) = p^{limit}\left[1 - \frac{r_l(t)}{r_l^0}\right] + p^{start}\left[\frac{r_1(t)}{r_l^0}\right], \tag{10}$$

where $r_l^0$ and $r_l(t)$ denotes the learning rate at the beginning and at the training step $t$, respectively. $p^{start}$ shows the starting prefactor, which goes to $p^{limit}$ at the end of the learning. Here, an exponential learning rate is considered as,

$$r_l(t) = r_l^0 \times d_r^{t/d_s}, \tag{11}$$

where $d_r$ and $d_s$ denote the decay rate and decay steps, respectively. Equations 7–11 pertains to DeePMD formulation.

## 2.4 Potential training

### 2.4.1 MTP

Our investigation commenced with an analysis of the convergence of the MTP towards density functional theory (DFT) energy and force metrics. A key aspect of this study involved conducting a grid search to optimize the MTP parameters. This search varied the potential levels from 6 to 24 and the $r_{cut}$ values from 5 Å to 8 Å at 1 Å intervals. This strategic approach enabled us to explore a wide range of potential configurations to ascertain the most effective one. This analysis was conducted using a selection of 1800 datasets that were not included in the fitting of the potential, as illustrated in Figure 1. A pivotal aspect of the convergence test was the assignment of greater weight to energy, reflecting its critical role in the overall accuracy of the potential.

The convergence analysis revealed that the energy per atom began showing signs of convergence at level 16. This was a key observation, indicating that the MTP was effectively capturing the energy characteristics consistent with DFT calculations from this level. Similarly, the force values also demonstrated significantly low root mean square error (RMSE) commencing at the same level, further affirming the reliability of the potential from level 16 onwards.

Given these findings, and to ensure a conservative and robust approach, we ultimately selected level 18, for the final model. This level was deemed to provide an optimal balance between complexity and accuracy. Additionally, $r_{cut}$ was set to 7 Å, for ensuring sufficient interaction range while maintaining computational efficiency. The minimum radius ($r_{min}$) was chosen to be 2 Å. This parameter is crucial for determining the minimum distance at which interactions are considered in the potential, thereby influencing the model's sensitivity to shorter-range forces.

For the MTP's training objective function, weights were thoughtfully assigned as follows: $w_e = 1$ for energy, $w_f = 0.01$ for force, and $w_s = 0.001$ for stress, with a priority on energy precision. This weighting strategy ensured a nuanced consideration of both force and stress, albeit with a lesser priority compared to energy, essential for crafting a nuanced and precise interatomic potential. The dataset leveraged for this purpose contained 40,000 frames, distributed in an 80:20 ratio between training and validation sets, to support effective model training and subsequent validation.

### 2.4.2 DeePMD

In our study, the DeePOT-SE model, as implemented in the DeePMD-kit package, was employed. The cut-off radius for the model was set to 6 Å, with the smoothing function commencing at 4 Å, ensuring a smooth transition and reducing potential artifacts in the force calculations.

The model's architecture included radial and angular embedded-atom neural networks, each featuring three hidden layers. These layers were composed of 10, 20, and 40 nodes, respectively, providing a robust framework for capturing the complex interatomic interactions. Additionally, the fitting networks were designed with three hidden layers, each containing 100 nodes.

Regarding the training parameters, the initial learning rate was set at 0.001, gradually decreasing to a final rate of $3.51 \cdot 10^{-8}$. This gradual reduction in the learning rate allowed for finer adjustments as the training progressed, leading to more accurate model predictions. The weighting factors for energies and forces were also carefully calibrated. Initially, the weights for energies were set at 0.02, increasing to 1 in the final stages, whereas the weights for forces started at 1,000 and were reduced to 1. This

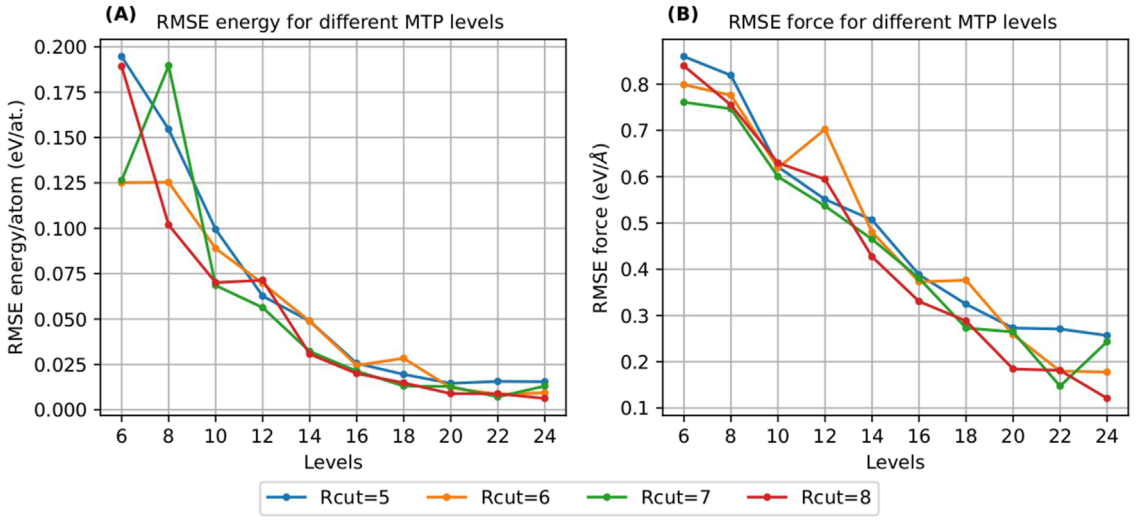


FIGURE 1
Convergence of MTP with respect to RMSE energy/atom **(A)** and RMSE force **(B)** with increasing MTP levels and cut-off radius (Rcut).

approach prioritized force accuracy in the initial stages of training and gradually shifted the focus towards energy accuracy.

It is noteworthy that virial data was not included in the training process. This decision was made to streamline the training and focus on the most critical aspects of the potential. The training was conducted over a substantial number of epochs, totaling 2,00,0000, to ensure comprehensive learning and optimization of the model parameters. The utilized dataset comprised 3,33,340 frames, divided into a training and validation set following an 80:20 ratio, facilitating effective model training and validation.

# 3 Results and discussion

## 3.1 Error analysis

The correlation between predictions from ML models and DFT calculations is pivotal in ascertaining the models' accuracy, particularly in simulating potential energy surfaces and material dynamics. Our study methodically evaluates this correlation for Nb-alloyed $\gamma$-TiAl and $\alpha_2$-$Ti_3Al$ phases using both MTP and DP models. Figures 2, 3 are instrumental in this analysis, showcasing the comparison of MTP and DP model predictions against DFT data, respectively.

The primary metrics for this comparison are energy per atom and the three components of force. For the MTP model, the recorded root mean square errors (RMSEs) are 0.0031 eV/atom for energy and 0.1285 eV/Å for the $x$-direction force (fx), 0.1329 eV/Å for the $y$-direction force (fy), and 0.1292 eV/Å for the $z$-direction force (fz). Conversely, the DP model exhibits RMSEs of 0.0011 eV/atom for energy, 0.0783 eV/Å for fx, 0.0795 eV/Å for fy, and 0.0820 eV/Å for fz. The DP model's RMSEs are notably lower than those of the MTP model, suggesting a marginally superior precision. Nevertheless, the energy and force RMSEs for both models are within acceptable ranges, confirming their effectiveness in reflecting DFT outcomes. Additionally, the RMSEs for energy per atom, fy, fy, and fz were computed for the training datasets and are presented in Table 1.

Both models' predictions exhibit a close alignment with the y = x line, highlighting their capacity to accurately reproduce the test dataset energies and atomic forces. This congruence is a robust indicator of the models' exceptional accuracy, which extends to untrained test data, suggesting their effectiveness in generalizing beyond the configurations they were trained on. The considered test data encompasses structures over a complete temperature range (1 K, 300 K, 500 K, 700 K and 900 K) and varying Nb concentrations (1–14 at.%). The lower RMSEs for both energy and force underscore the DP model's superior ability to achieve DFT-level accuracy compared to the MTP model. This indicates the potential of the DP model as a more precise tool for simulating the behaviors of Nb-doped $\gamma$-TiAl and $\alpha_2$-$Ti_3Al$ phases, backed by its comparative closeness to DFT calculations.

## 3.2 MD simulations

### 3.2.1 Energy volume curve

To augment the validity of the DeePMD and MTP potentials, this study meticulously examines the energy-volume relationships obtained using the Murnaghan fit in Nb-alloyed $\alpha_2$-$Ti_3Al$ and $\gamma$-TiAl phases. Illustrations of these relationships are effectively depicted in Figure 4. Remarkably, the outcomes from MD simulations employing DeePMD and MTP exhibit exceptional congruence with those derived from DFT calculations. This alignment highlights the adeptness of the trained potentials in precisely capturing the energy-volume characteristics inherent to these materials.

Table 2 shows the equilibrium volume predicted by DFT, MTP and DeePMD for $\alpha_2$-$Ti_3Al$ and $\gamma$-TiAl. For the $\alpha_2$-$Ti_3Al$, equilibrium volumes predicted by DFT, MTP, and DeePMD are respectively 15.88 $Å^3$, 16.40 $Å^3$ and 14.52 $Å^3$. In a similar vein, for $\gamma$-TiAl

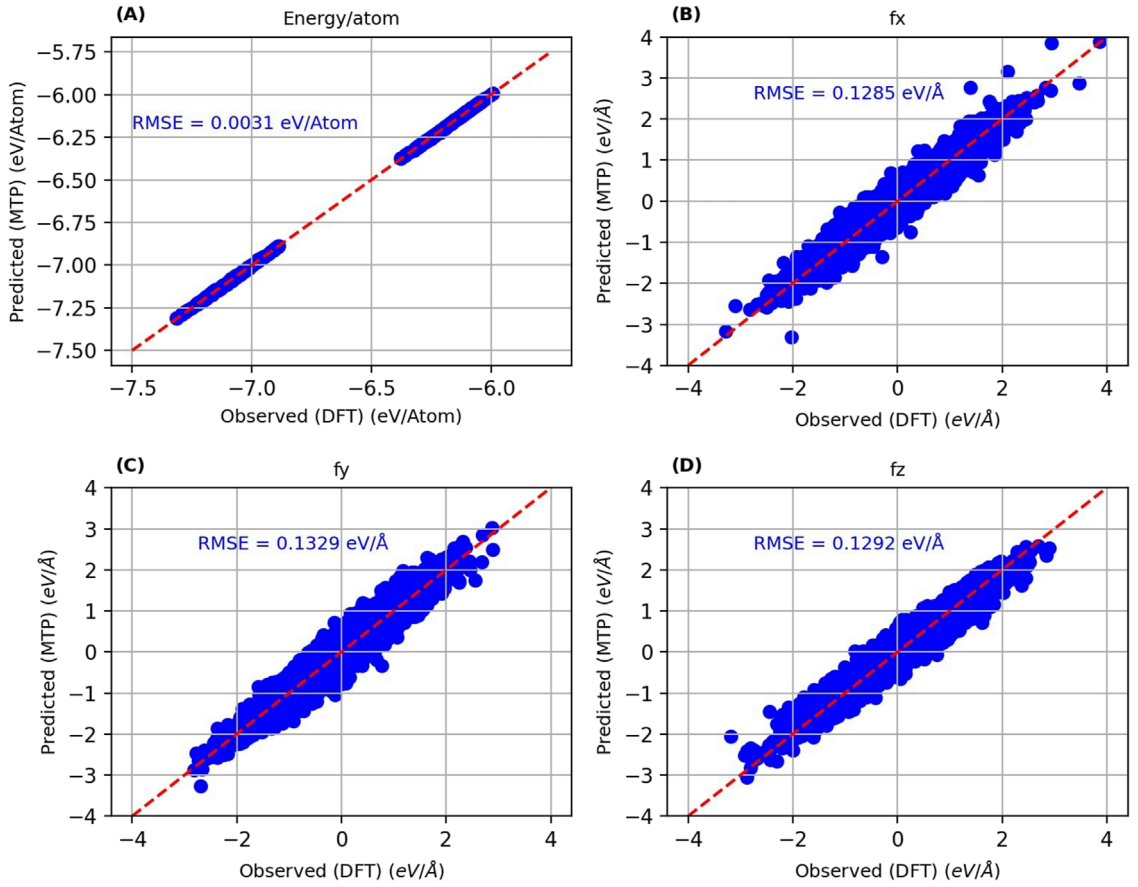


FIGURE 2
Parity plots of MTP predicted energy per atom **(A)**, x-component of force **(B)**, y-component of force **(C)** and z-component of force **(D)** against the corresponding DFT values.

phase, the corresponding values are 16.22 $Å^3$, 15.76 $Å^3$ and 15.46 $Å^3$. Notably, the equilibrium volume predictions by MTP align more closely with those from DFT than do those by DeePMD for both phases.

The lattice constants predicted by DFT, MTP and DeePMD for $\alpha_2$-$Ti_3Al$ and $\gamma$-TiAl are compared to corresponding experimental values (PEARSON, 1958; He et al., 1997) in Table 2. For the $\alpha_2$-$Ti_3Al$ phase, MTP predicts lattice constants of a = 5.683 Å and c = 4.633 Å. These closely match the DFT-calculated values of a = 5.625 Å and c = 4.586 Å and experimental values (PEARSON, 1958) of a = 5.770 Å and b = 4.620 Å. Conversely, DeePMD predicts a = 5.453 Å and c = 4.446 Å, slightly diverging from the DFT lattice parameters. The equilibrium lattice constants for $\gamma$-TiAl as forecasted by MTP–a = 3.910 Å and c = 4.099 Å – exhibit a striking resemblance to the DFT-determined values of a = 3.950 Å and c = 4.140 Å whereas the experimental values (He et al., 1997) are a = 3.998 Å and c = 4.067 Å. The DeePMD predictions, a = 3.910 Å and c = 4.099 Å, are identical to those of MTP, showcasing their close alignment with DFT values.

Accurate energy prediction in competitive phases is vital to avert unphysical phase segregation during MD simulations. Therefore, the integration of machine learning potentials like DeePMD and MTP notably enhances the structural analysis and prediction capabilities in Nb-alloyed $\alpha_2$-$Ti_3Al$ and $\gamma$-TiAl phases, underscoring their significance in the realm of advanced materials research. In terms of equilibrium volume and lattice constant prediction, MTP demonstrates superior performance compared to DeePMD.

### 3.2.2 Elastic constants

Next we assessed the elastic constants of $\alpha_2$-$Ti_3Al$ and $\gamma$-TiAl alloys utilizing the different computational methodologies DFT, MTP, and DeePMD. The outcomes, quantified in gigapascals (GPa), provide a detailed comparison of the mechanical attributes predicted by these models against established experimental values (Tanaka and Koiwa, 1996; Tanaka, 1996) in Table 2.

For the $\alpha_2$-$Ti_3Al$ alloy, notable discrepancies emerge in the elastic constants across the computational approaches compared to experimental standards (Tanaka and Koiwa, 1996). Specifically, the DeePMD's $C_{11}$ prediction of 339 GPa significantly overshoots the figures from DFT (157 GPa), MTP (147 GPa), and experimental data (183 GPa), indicating an overestimation of longitudinal stiffness by DeePMD. The variations in $C_{12}$ and $C_{33}$, which reflect differences in predicted interatomic bond strengths and compressibility along distinct crystallographic directions, are particularly striking, with DFT (103 GPa and 219 GPa) and experimental (89 GPa and 225 GPa) benchmarks. The DeePMD's divergence in $C_{13}$, which measures axial-longitudinal strain

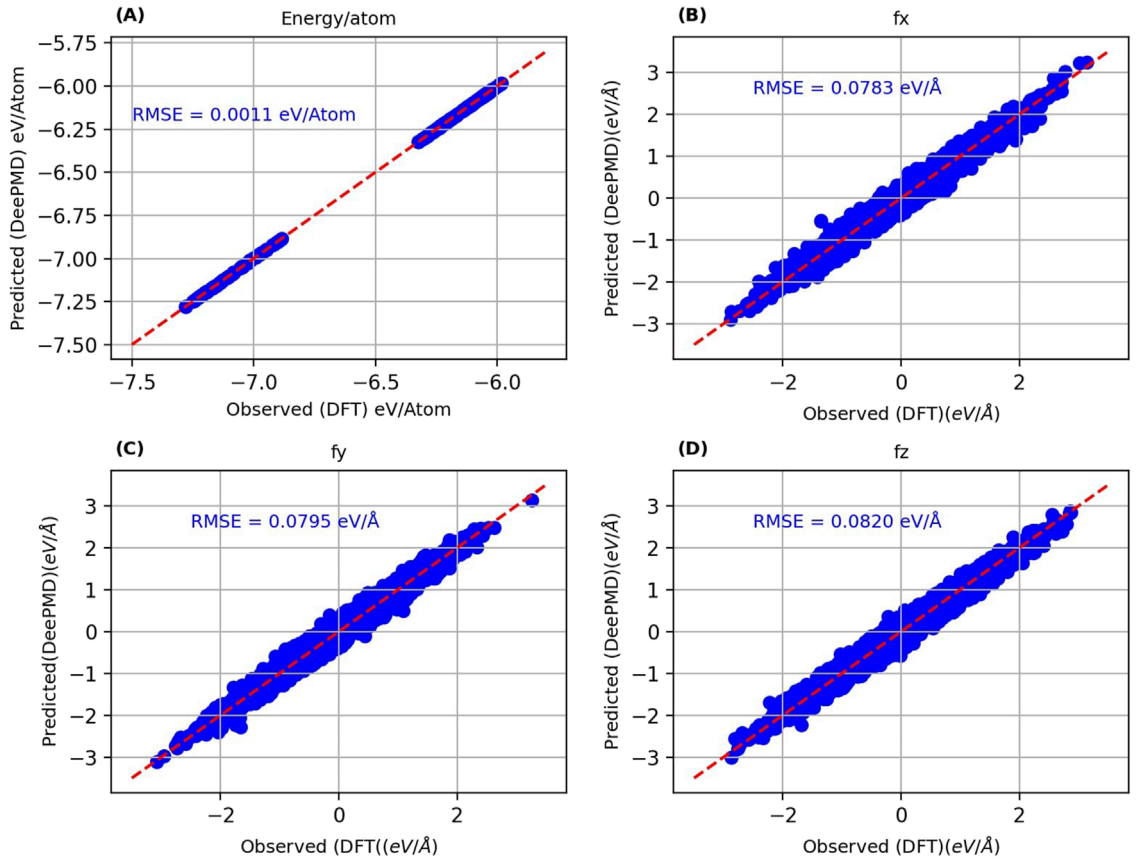


FIGURE 3
Parity plots of DeePMD predicted energy per atom **(A)**, x-component of force **(B)**, y-component of force **(C)** and z-component of force **(D)** against the corresponding DFT values.

**TABLE 1** Comparison of RMSE values of energy/atom, fx, fy, and fz for MTP and DeePMD using training data.

| Potential | RMSE | | | |
|---|---|---|---|---|
| | Energy/atom (eV/atom) | fx (eV/Å) | fy (eV/Å) | fz (eV/Å) |
| MTP | 0.00303 | 0.13365 | 0.13705 | 0.13188 |
| DeePMD | 0.00107 | 0.06463 | 0.06947 | 0.06886 |

interactions, sharply contrasts with DFT's 74 GPa and the experimental value of 63 GPa. Additionally, the $C_{44}$ constant, crucial for evaluating resistance to shear deformation, shows variation, with MTP predicting 34 GPa against DFT's 46 GPa and experimental findings of 64 GPa. It is noteworthy that the $C_{66}$ constant is not applicable for the $\alpha_2$-$Ti_3Al$ phase in this analysis.

In the analysis of the $\gamma$-TiAl alloy, the elastic constants exhibit significant variances across the computational techniques, juxtaposed with experimental findings (Tanaka, 1996). The $C_{11}$ constant, indicative of the material's longitudinal rigidity, shows a broad range of values, with DFT's prediction of 179 GPa closely mirroring the experimental value of 187 GPa, in contrast to the lower estimations of 146 GPa by both MTP and DeePMD. Conversely, the shear-related $C_{44}$ constant demonstrates minimal variation among the models, aligning closely with the experimental measure of 109 GPa and DFT value of 102 GPa.

Table 3 presents a comparison of the elastic constants for $\alpha_2$-$Ti_3Al$ and $\gamma$-TiAl at 300 K, 500 K, 700 K, and 900 K. As expected, the elastic constants for both $\alpha_2$-$Ti_3Al$ and $\gamma$-TiAl decrease with increasing temperature, consistent with findings reported in Qi et al. (2023). Our calculated values have been compared to available experimental data (He et al., 1997; Tanaka, 1996) for $\gamma$-TiAl; (Tanaka et al., 1996) for $\alpha_2$-$Ti_3Al$), though it is important to note that experimental values are not available for $\gamma$-TiAl at 900 K and for $\alpha_2$-$Ti_3Al$ at 500 K, 700 K, and 900 K. Moreover, the $C_{66}$ constant does not apply to the $\alpha_2$-$Ti_3Al$ phase in this analysis. The discrepancies observed in the elastic constants in Table 2 are also present here; however, the overall trend of decreasing elastic constants with

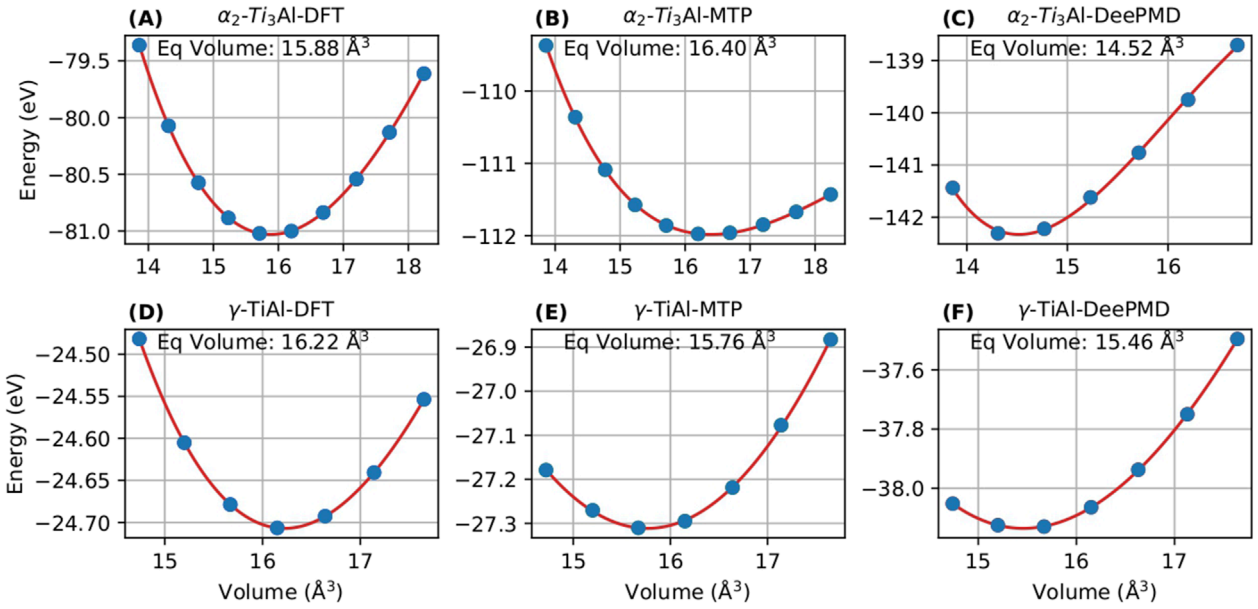


FIGURE 4
Energy-volume curve of $\alpha_2$-$Ti_3Al$ **(A–C)** and $\gamma$-TiAl **(D–F)** phases computed using DFT, MTP and DeePMD methods.

TABLE 2 Comparison of lattice constants (a, c), equilibrium volume ($V_0$) and elastic constants for $\gamma$-TiAl and $\alpha_2$-$Ti_3Al$ using DFT, MTP, and DeePMD methods along with the experimental values. Lattice constants are in Å, equilibrium volume in Å$^3$, and elastic constants are in GPa.

| Quantities | $\alpha_2$-$Ti_3Al$ | | | | $\gamma$-TiAl | | | |
|---|---|---|---|---|---|---|---|---|
| | DFT | MTP | DeePMD | Exp[a,b] | DFT | MTP | DeePMD | Exp[c,d] |
| a | 5.625 | 5.683 | 5.453 | 5.770 | 3.950 | 3.910 | 3.910 | 3.998 |
| c | 4.586 | 4.633 | 4.446 | 4.620 | 4.140 | 4.099 | 4.099 | 4.067 |
| $V_0$ | 15.88 | 16.40 | 14.52 | N/A | 16.22 | 15.76 | 15.46 | N/A |
| $C_{11}$ | 157 | 147 | 339 | 183 | 179 | 146 | 146 | 187 |
| $C_{12}$ | 103 | 63 | 204 | 89 | 121 | 48 | 111 | 75 |
| $C_{33}$ | 219 | 165 | 261 | 225 | 177 | 279 | 65 | 182 |
| $C_{13}$ | 74 | 10 | 155 | 63 | 94 | 111 | 124 | 75 |
| $C_{44}$ | 46 | 34 | 50 | 64 | 102 | 88 | 96 | 109 |
| $C_{66}$ | N/A | N/A | N/A | N/A | 75 | 81 | 109 | 81 |

[a]Tanaka and Koiwa, 1996.
[b]PEARSON, 1958.
[c]Tanaka, 1996.
[d]He et al., 1997.

increasing temperature for both phases remains consistent with the previous studies mentioned.

The observed disparities in elastic constants among the DFT, MTP, and DeePMD methodologies, relative to experimental data (Tanaka and Koiwa, 1996; Tanaka, 1996), highlight the intricate challenges of accurately simulating material behaviors. These differences can be attributed to the unique features of each approach, including DFT's detailed electron correlation handling, MTP's potential function structure, and DeePMD's reliance on extensive training datasets and neural network designs. Our analysis underscores the critical importance of selecting appropriate computational strategies tailored to specific material characteristics and the need for cautious interpretation of computational findings in materials science. This study reinforces the indispensable role of

10.3389/fmats.2024.1466793

TABLE 3 Comparison of elastic constants of $\alpha_2$-$Ti_3Al$ and $\gamma$-TiAl at 300 K, 500 K, 700 K and 900 K using MTP, DeePMD and experimental methods. Elastic constants are measured in GPa.

| Elastic constants | Temperature (K) | $\alpha_2$-$Ti_3Al$ | | | $\gamma$-TiAl | | |
|---|---|---|---|---|---|---|---|
| | | MTP | DeePMD | Exp[a] | MTP | DeePMD | Exp[b,c] |
| $C_{11}$ | 300 | 135.3 | 314.5 | 156.9 | 145.5 | 134.8 | 181.8 |
| | 500 | 119.4 | 287.0 | N/A | 143.3 | 130.1 | 177.2 |
| | 700 | 109.6 | 251.0 | N/A | 140.6 | 126.0 | 170.5 |
| | 900 | 106.4 | 246.6 | N/A | 139.4 | 119.5 | N/A |
| $C_{12}$ | 300 | 57.3 | 203.2 | 87.4 | 46.8 | 107.9 | 73.5 |
| | 500 | 54.2 | 190.7 | N/A | 44.3 | 91.5 | 74.9 |
| | 700 | 48.6 | 189.3 | N/A | 43.3 | 88.9 | 73.5 |
| | 900 | 39.4 | 182.7 | N/A | 42.3 | 80.1 | N/A |
| $C_{13}$ | 300 | 9.3 | 140.4 | 61.5 | 110.9 | 118.8 | 73.5 |
| | 500 | 8.0 | 120.4 | N/A | 110.4 | 117.6 | 72.5 |
| | 700 | 6.5 | 100.2 | N/A | 110.3 | 116.6 | 71.7 |
| | 900 | 6.2 | 103.0 | N/A | 108.3 | 112.7 | N/A |
| $C_{33}$ | 300 | 164.2 | 218.7 | 216.3 | 46.8 | 64.7 | 174.0 |
| | 500 | 163.4 | 211.5 | N/A | 46.5 | 63.8 | 170.0 |
| | 700 | 161.7 | 202.4 | N/A | 44.3 | 62.0 | 163.1 |
| | 900 | 161.3 | 193.9 | N/A | 43.3 | 60.6 | N/A |
| $C_{44}$ | 300 | 33.5 | 46.8 | 61.5 | 87.7 | 95.9 | 103.1 |
| | 500 | 32.4 | 45.9 | N/A | 86.6 | 95.9 | 98.0 |
| | 700 | 32.3 | 42.1 | N/A | 85.6 | 94.1 | 94.2 |
| | 900 | 31.3 | 38.6 | N/A | 83.3 | 92.2 | N/A |
| $C_{66}$ | 300 | N/A | N/A | N/A | 80.6 | 109.5 | 71.6 |
| | 500 | N/A | N/A | N/A | 80.6 | 107.0 | 66.1 |
| | 700 | N/A | N/A | N/A | 78.3 | 106.4 | 62.9 |
| | 900 | N/A | N/A | N/A | 75.0 | 104.9 | N/A |

[a]Tanaka et al., 1996
[b]He et al., 1997
[c]Tanaka, 1996.

experimental validation in confirming the veracity of computational predictions.

### 3.2.3 Radial distribution function

The radial distribution function (RDF) serves as an instrumental tool for analyzing the structural properties of materials. In our study, illustrated in Figures 5, 6, we present a comparative analysis of RDFs predicted by MTP and DeePMD against those obtained from AIMD for Nb in $\alpha_2$-$Ti_3Al$. Additionally, Figures 7, 8 show a similar comparison for Nb in $\gamma$-TiAl. It is important to note that the structural instances used for RDF analysis with DFT were not part of the training sets for either the MTP or DeePMD models. The agreement between the outcomes underscores the dependability of DeePMD and MTP models in probing the structure of Nb-alloyed $\alpha_2$-$Ti_3Al$ and $\gamma$-TiAl phases.

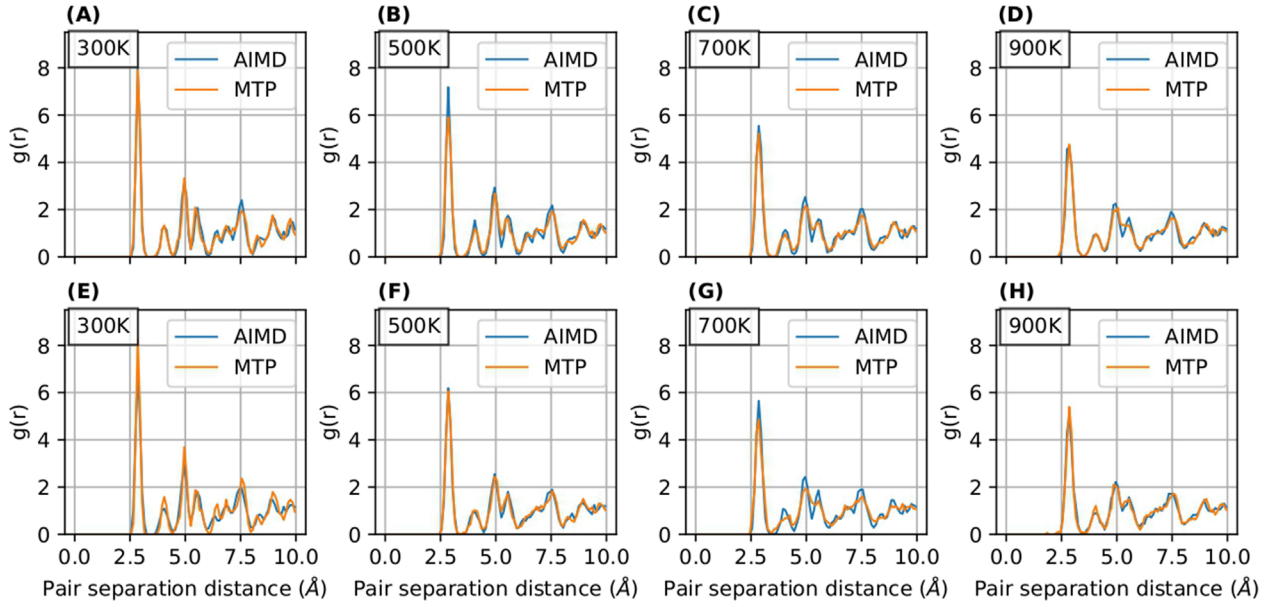


FIGURE 5
RDF curves for $\alpha_2$-$Ti_3Al$ obtained using MTP potential for 2.3 at.% Nb **(A–D)** and 6.3 at.% Nb **(E–H)** models.

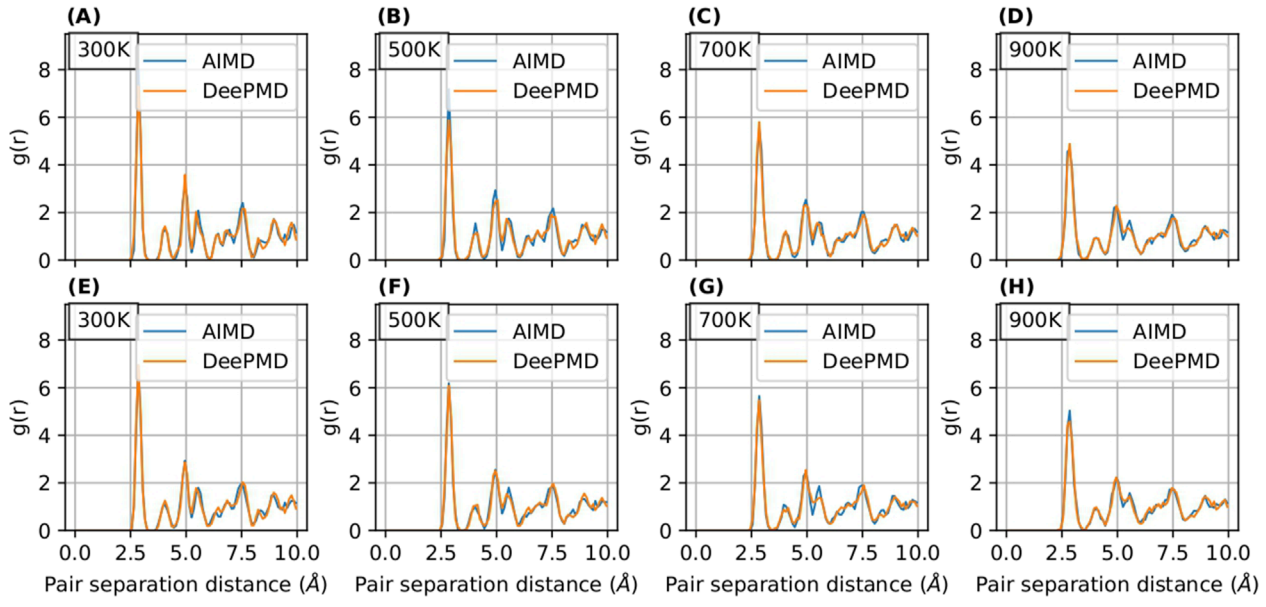


FIGURE 6
RDF curves for $\alpha_2$-$Ti_3Al$ obtained using DeePMD potential for 2.3 at.% Nb **(A–D)** and 6.3 at.% Nb **(E–H)** models.

Notably, the RDFs for $\gamma$-TiAl from AIMD exhibited a closer match with the ML potentials compared to those for $\alpha_2$-$Ti_3Al$. This could be attributed to the ML models encountering challenges in accurately replicating structures when two different phases are present. In the case of $\alpha_2$-$Ti_3Al$, we observed a diminishing correlation between the RDFs from AIMD and ML potentials with increasing temperature, as demonstrated in Figure 5G (6.3 at.% Nb) and 6G (6.3 at.% Nb). Furthermore, at 300 K, the RDF for 7.4 at.% Nb in $\gamma$-TiAl (Figure 8E) showed a discrepancy between AIMD and DeePMD, while the MTP model maintained a good correlation for the same scenario. These observations highlight the nuanced performance of ML potentials in different phase contexts and temperature conditions.

Additionally, we examined the scalability of the developed potentials with system sizes, as detailed in

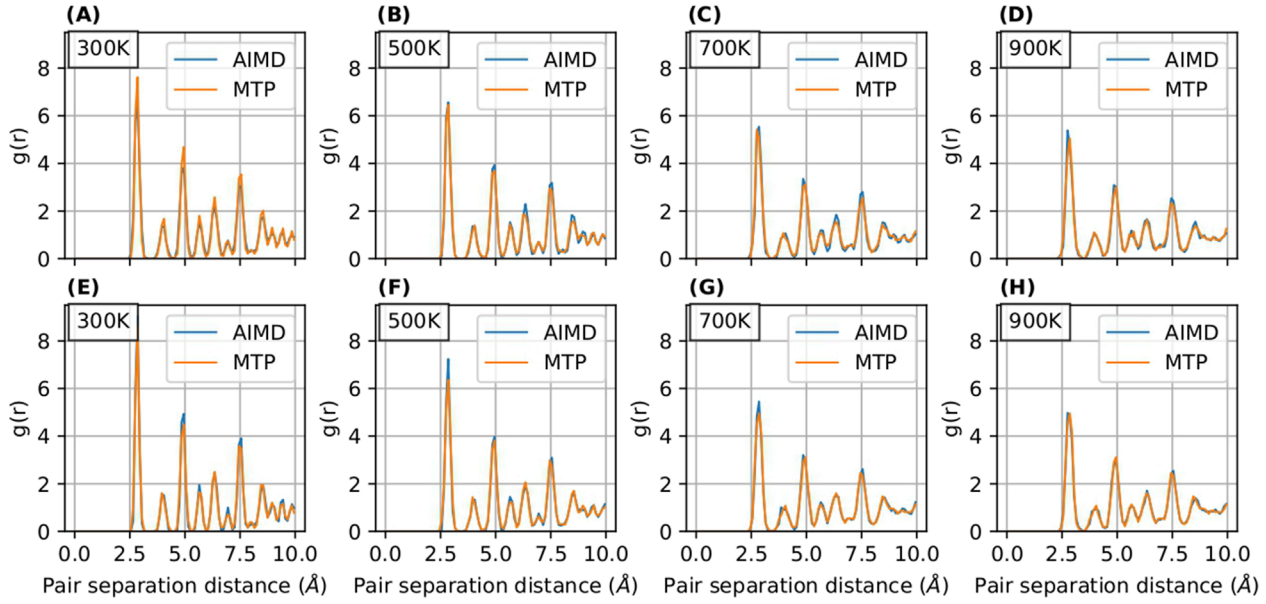


FIGURE 7
RDF curves for $\gamma$-TiAl obtained using MTP potential for 1.9 at.% Nb **(A–D)** and 7.4 at.% Nb **(E–H)** models.

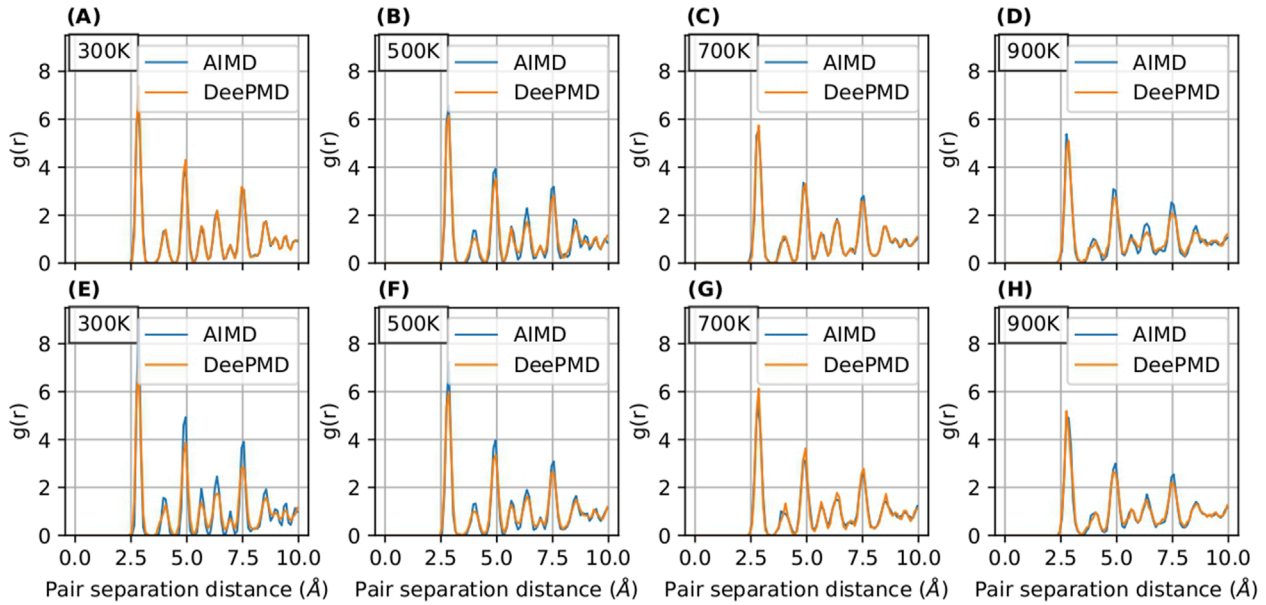


FIGURE 8
RDF curves for $\gamma$-TiAl obtained using DeePMD potential for 1.9 at.% Nb **(A–D)** and 7.4 at.% Nb **(E–H)** models.

Supplementary Figures S1–S4 in the Supplementary Material in Section 2. For further insights, please refer to this section in the Supplementary Material. Our study also extended to comparing RDFs calculated by DFT, MTP, and DeePMD for a specific case of 14.8 at.% Nb concentration, which exceeds the training data's Nb concentration range. These results are documented in the Supplementary Material in Section 3, providing valuable perspectives on the models' performance beyond their initial training scope.

### 3.2.4 Specific heat capacity and thermal expansion

To assess the predictive capability of trained MTP and DeePMD potentials at finite temperatures, this section reports the computation of specific heat capacity ($C_V$) for 3.1 at.% Nb structures of $\alpha_2$-$Ti_3Al$ and $\gamma$-TiAl and thermal expansion coefficients ($\alpha_a$ and $\alpha_c$) for $\alpha_2$-$Ti_3Al$ and $\gamma$-TiAl as the temperature increases. For the computation of specific heat capacity we have used phonopy (Togo et al., 2023; Togo, 2023).

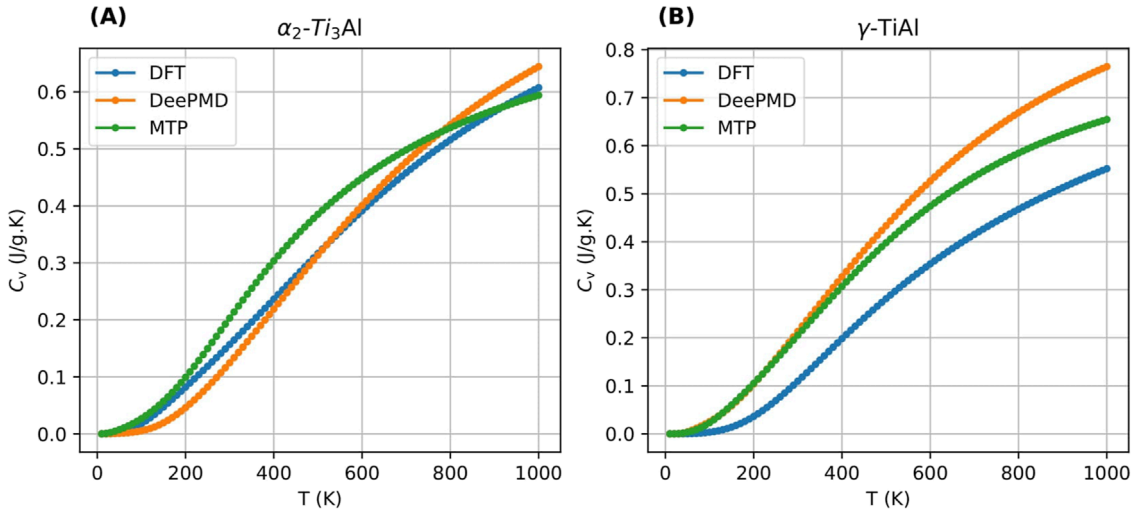


FIGURE 9
Comparison of specific heat capacity computed using MTP, DeePMD and MTP for 3.1 at.% Nb cases for $\alpha_2$-$Ti_3Al$ **(A)** and $\gamma$-TiAl **(B)**.

Figures 9A, B illustrate the comparisons of $C_V$ values calculated using DeePMD and MTP against those derived from DFT for 3.1 at.% Nb of $\alpha_2$-$Ti_3Al$ and $\gamma$-TiAl, respectively. It is observed that $C_V$ progressively increases with temperature across all methods, reflecting the system's access to more degrees of freedom at higher temperatures. For $\alpha_2$-$Ti_3Al$, the alignment of the curves from the three methods is notably good. Specifically, the DeePMD results closely mirror the DFT outcomes, whereas the MTP results show minor deviations between 177 K and 777 K, aligning better at temperatures beyond this range. For quantitative clarity, at 200 K, $C_V$ values are 0.045 J/g.K, 0.099 J/g.K, and 0.082 J/g.K for DeePMD, MTP, and DFT, respectively; at 600 K, they are 0.401 J/g.K, 0.449 J/g.K, and 0.392 J/g.K; and at 1000 K, they are 0.647 J/g.K, 0.595 J/g.K, and 0.608 J/g.K. It should be noted that the training set for these potentials only included structures up to 900 K. For $\gamma$-TiAl, although the MTP and DeePMD predictions initially closely match, they begin to diverge slightly beyond 288 K. Quantitative values at 200 K are 0.104 J/g.K for both DeePMD and MTP, and 0.355 J/g.K for DFT; at 600 K, the values are 0.525 J/g.K, 0.473 J/g.K, and 0.352 J/g.K; and at 1000 K, they are 0.765 J/g.K, 0.655 J/g.K, and 0.554 J/g.K.

In terms of thermal expansion, we computed the coefficients $\alpha_a$ and $\alpha_c$ corresponding to lattice parameters a and c at temperatures up to 900 K (Figure 10) for $\alpha_2$-$Ti_3Al$ and $\gamma$-TiAl. These values were compared with experimental results for $\gamma$-TiAl (He et al., 1997) and DFT calculations for $\alpha_2$-$Ti_3Al$ (Holec et al., 2019). It is important to note that low-temperature behaviors, often influenced by quantum effects, are not typically well captured by classical interatomic potentials. Both $\alpha_a$ and $\alpha_c$ typically increase with temperature, aiming to stabilize at higher temperatures. Experimental and DFT reference values are only available up to 750 K. At higher temperatures, $\alpha_a$ and $\alpha_c$ calculated using DeePMD are closer to these reference values, whereas MTP underpredicts these coefficients for both phases. Thus, DeePMD proves to be more accurate in predicting thermal expansion coefficients than MTP.

### 3.2.5 Tension test

Here, we aimed to assess the capabilities of the MTP and DeePMD potentials in capturing the thermo-mechanical characteristics of specific materials. To achieve this, we simulated uniaxial tension tests on chosen samples, applying a strain rate of $10^9$ $s^{-1}$. The stress-strain curves obtained from these tension tests, utilizing both MTP and DeePMD potentials for the $\alpha_2$-$Ti_3Al$ and $\gamma$-TiAl phases, are illustrated in Figure 11. Table 4 presents a comparative analysis of ultimate tensile strength (UTS) values for these materials.

We focused on comparing the UTS of the intermetallic phases to gauge the accuracy of mechanical property predictions. For the $\alpha_2$-$Ti_3Al$ phase, MTP demonstrated consistency in UTS with increase in Nb concentration. Conversely, with the DeePMD potential, the UTS decreased as the Nb concentration increased. In the $\gamma$-TiAl phase, an increase in Nb concentration typically led to a rise in UTS with DeePMD, whereas with MTP, a decrease in UTS was observed with increasing Nb, except for the 7.4 at.% Nb scenario. The results of tension curves for $\gamma$-TiAl with Nb introduction using DeePMD shows a discrepancy with that presented in Lu et al. (2023).

Further insights into the nanomechanical behavior during uniaxial tension tests in the $\alpha_2$-$Ti_3Al$ and $\gamma$-TiAl phases are provided in Figure 12. These figures employ color coding to depict the centrosymmetry parameter (CSP), which helps identify local lattice distortions and hence, defects. For the $\alpha_2$-$Ti_3Al$ phase, the strain levels at which defects appeared remained relatively constant across different Nb concentrations with MTP, but showed a decrease with increasing Nb concentration in DeePMD, except in the case of 7 at.% Nb. These findings are in agreement with the stress-strain curves of depicted in Figures 11A, B. In the $\gamma$-TiAl phase, the strain threshold for defect formation decreased with increasing Nb concentration using MTP, while it increased with increasing Nb concentration in DeePMD. This observation aligns with the stress-strain data shown in Figures 11C, D.

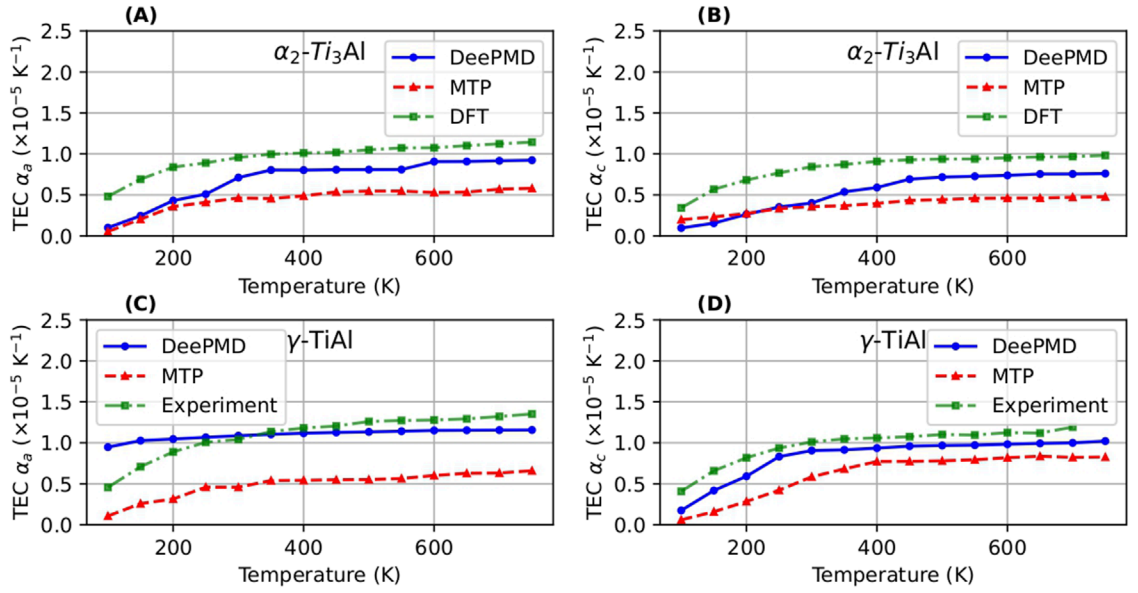


FIGURE 10
Thermal expansion coefficient (TEC) computed using DeePMD and MTP compared with the DFT values (Holec et al., 2019) and experimental values (He et al., 1997) for $\alpha_2$-$Ti_3Al$ **(A, B)** and $\gamma$-TiAl **(C, D)** respectively.

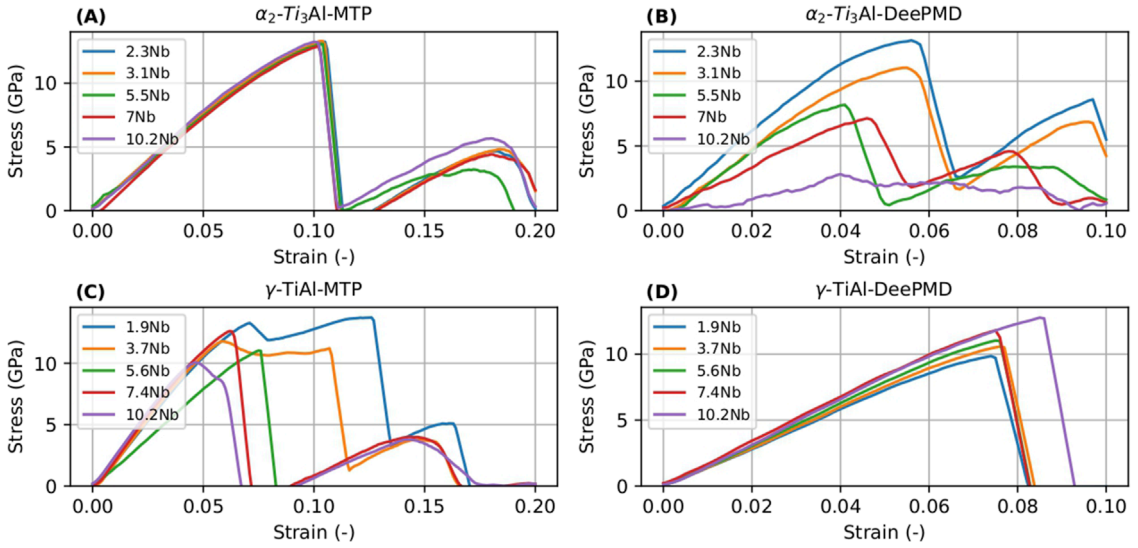


FIGURE 11
Stress-strain curves for $\alpha_2$-$Ti_3Al$ **(A, B)** and $\gamma$-TiAl **(C, D)** with varying Nb concentration computed using MTP and DeePMD potentials.

### 3.2.6 Generalized stacking fault energy

This section evaluates the generalized stacking fault energy (GSFE) of $\gamma$-TiAl and $\alpha_2$-$Ti_3Al$ using both DeePMD and MTP potentials. Our analysis compares these findings with results derived from DFT and other referenced studies. Specifically, we examine studies such as Qi et al. (2023), which utilized the MTP potential, and (Lu et al., 2023), which employed the DeePMD method, where the values are available only for $\gamma$-TiAl. We used atomman (atomistic manipulation toolkit) (Becker et al., 2013; Hale et al., 2018) for the computation of stacking fault energy.

For $\gamma$-TiAl, dislocation glide occurs on the {111} close-packed planes, which are susceptible to three distinct types of stacking faults: intrinsic stacking fault (SISF), antiphase boundary (APB), and complex stacking fault (CSF). CSF is associated with ordinary $\langle\bar{1}10]/2$ dislocations, while SISF and APB are linked to $\langle\bar{1}10]$ and $\langle11\bar{2}]/2$ super-dislocations. Figures 13A–D shows the $\gamma$-lines along $[11\bar{2}]$ direction for $\gamma$-TiAl using both MTP and DeePMD. The energy values are documented in Table 5. MTP models generally align with the DFT and other referenced values for CSF, though MTP tends to overestimate SISF energy, in agreement with findings

TABLE 4 Comparison of UTS values for $\alpha_2$-$Ti_3Al$ and $\gamma$-TiAl using MTP and DeePMD potentials.

| $\alpha_2$-$Ti_3Al$ | | | $\gamma$-TiAl | | |
|---|---|---|---|---|---|
| Model (at.%) | MTP (GPa) | DeePMD (GPa) | Model (at.%) | MTP (GPa) | DeePMD (GPa) |
| 2.3 Nb | 13.48 | 13.47 | 1.9 Nb | 13.86 | 10.06 |
| 3.1 Nb | 13.50 | 11.36 | 3.7 Nb | 12.05 | 10.78 |
| 5.5 Nb | 13.25 | 8.41 | 5.6 Nb | 11.09 | 11.23 |
| 7.0 Nb | 13.07 | 7.47 | 7.4 Nb | 12.82 | 12.11 |
| 10.2 Nb | 13.42 | 3.14 | 10.2 Nb | 10.21 | 13.13 |

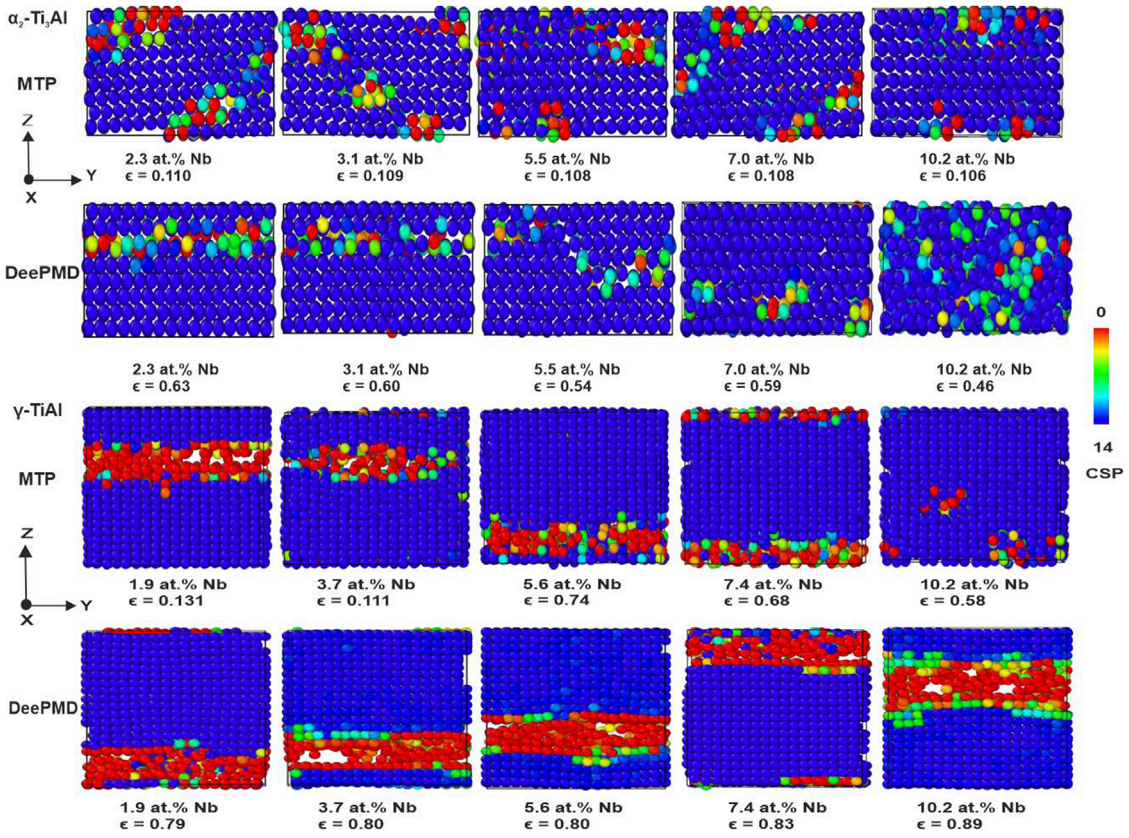


FIGURE 12
$\alpha_2$-$Ti_3Al$ (first and second rows) and $\gamma$-TiAl (third and fourth rows) phases deformed at 300 K under uniaxial tension tests performed using the MTP potential and DeePMD potential.

from Qi et al. (2023). Conversely, DeePMD tends to align the SISF values more closely with DFT, while both models underpredict APB energy. Notably, the sequence SISF < CSF < APB remains consistent across both computational approaches as reported in Qi et al. (2023) and Lu et al. (2023). Generally, a higher GSFE indicates increased resistance and reduced mobility of dislocations, which directly contributes to the strengthening behavior in nanomaterials, whereas a lower GSFE suggests higher mobility of dislocations and improved ductility. With an increase in Nb concentration, there is a noticeable decline in the energies for SISF, CSF, and APB for MTP, whereas DeePMD shows an increase (except for 4 at.% Nb case for CSF). Zhao et al. (2024) reported that an increase in Nb concentration reduced the stacking fault energies in the $\gamma$-TiAl phase. Similar findings were reported by Dumitraschkewitz et al. (2017), suggesting that MTP predicts this trend well. However, DeePMD presents a discrepancy where Nb alloying has increased the stacking fault energy for $\gamma$-TiAl, although this aligns with the tension curves in Figures 11C, D.

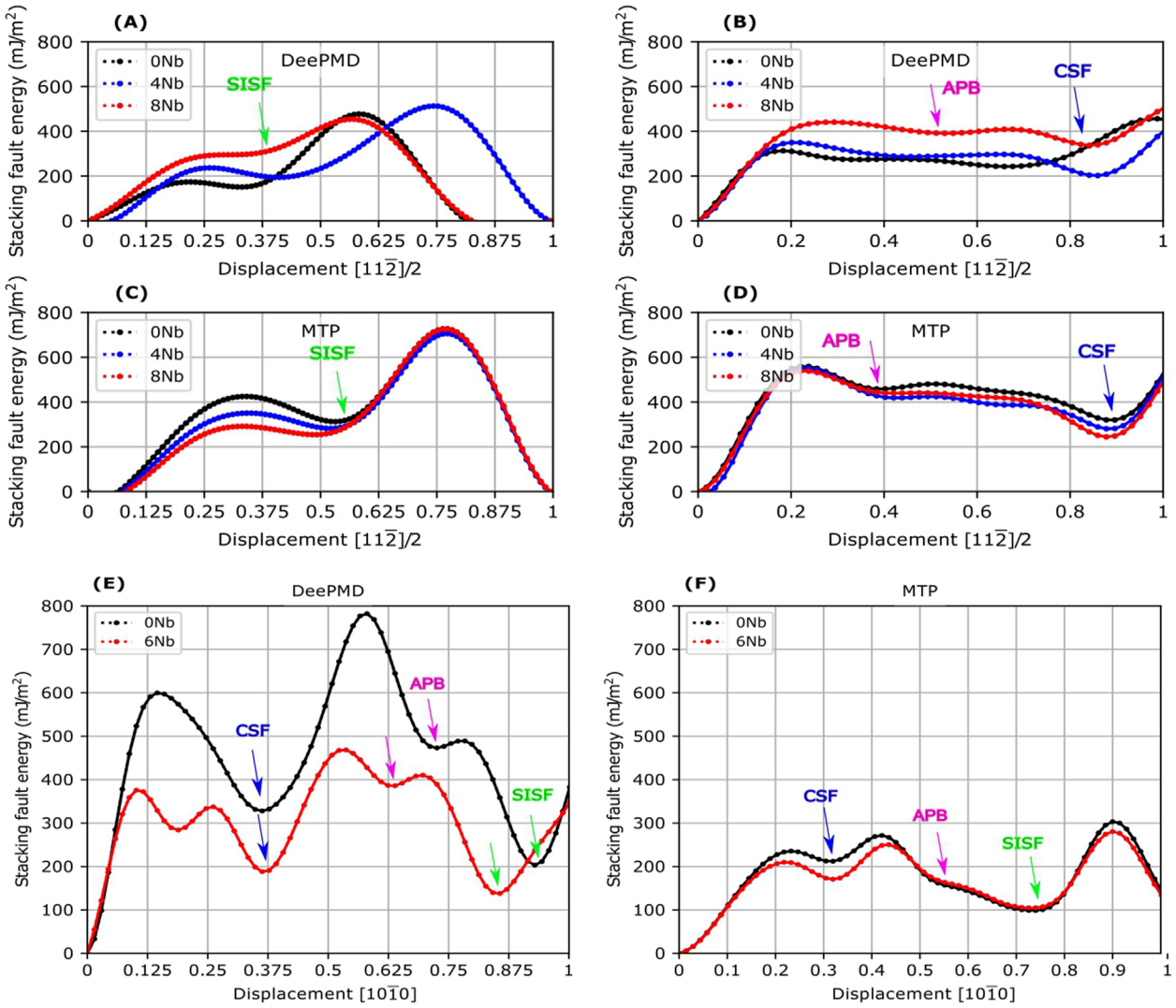


FIGURE 13
The generalized stacking fault energy (GSFE) on the {111} plane of $\gamma$-TiAl **(A–D)** and {0001} plane of $\alpha_2$-$Ti_3Al$ **(E–F)** predicted by MTP and DeePMD. **(A, C)** The $\gamma$-line along the $\langle 11\bar{2}]$ direction passing through the SISF. **(B, D)** The $\gamma$-line along the $\langle 11\bar{2}]$ direction passing through the APB and CSF. **(E, F)** The $\gamma$-line along the $[10\bar{1}0]$ direction passing through SISF, CSF and APB.

Turning to the $\alpha_2$-$Ti_3Al$ phase, characterized by hexagonal symmetry and various slip systems, our analysis primarily focuses on the fundamental {0001} plane. Figures 13E, F shows the $\gamma$-line along $[01\bar{1}0]$ direction obtained using MTP and DeePMD and the corresponding energy values are listed in Table 5. The results for $\alpha_2$-$Ti_3Al$ show less consistency with DFT and referenced values (Qi et al., 2023) compared to $\gamma$-TiAl. MTP predictions for SISF align with DFT and referenced data (Qi et al., 2023), whereas DeePMD tends to slightly overestimate SISF and notably overpredict APB energy. However, DeePMD predictions for CSF energy are closer to DFT and reference values. With an increase in Nb concentration, SISF, APB, and CSF energies decrease with DeePMD, consistent with Figures 11A, B. However, MTP shows minimal change in APB and SISF values, with only a slight decrease in SISF upon Nb introduction, indicating a minimal impact of Nb alloying on the material's strength, as corroborated by the data in Table 4.

We have observed that, except for DeePMD for $\gamma$-TiAl, Nb alloying generally reduces the stacking fault energy in both phases, indicating improved ductility. Our previous work (Chandran et al., 2024) demonstrated that Nb alloying enhances dislocation density and thus overall ductility, albeit at the expense of reduced strength. The stacking fault energy computations presented here align with this finding except for DeePMD for $\gamma$-TiAl.

## 3.3 Comparison of performance of MTP and DeePMD

Here, we conducted a thorough assessment of the computational efficiency in MD simulations, focusing on DeePMD and MTP potentials. Figure 14 provides a graphical representation of simulation performance measured in hours per nanosecond

TABLE 5 Comparison of generalized stacking fault energies values for $\gamma$-TiAl and $\alpha_2$-$Ti_3Al$ using MTP and DeePMD potentials.

| Phases | Fault energy | Nb conc (at.%) | DFT | MTP | Ref[a] | DeePMD | Ref[b] |
|---|---|---|---|---|---|---|---|
| $\gamma$-TiAl | SISF ($mJ/m^2$) | 0Nb | 182[a], 194[c] | 312 | 322 | 149 | 129 |
| | | 4Nb | — | 285 | — | 193 | — |
| | | 8Nb | — | 251 | — | 294 | — |
| | APB ($mJ/m^2$) | 0Nb | 560[d], 623[b] | 461 | 611 | 280 | 649 |
| | | 4Nb | — | 451 | — | 288 | — |
| | | 8Nb | — | 428 | — | 397 | — |
| | CSF ($mJ/m^2$) | 0Nb | 356[a], 372[e] | 324 | 372 | 239 | 439 |
| | | 4Nb | — | 281 | — | 201 | — |
| | | 8Nb | — | 247 | — | 338 | — |
| $\alpha_2$-$Ti_3Al$ | SISF ($mJ/m^2$) | 0Nb | 93[a], 104[b] | 97 | 84 | 206 | — |
| | | 6Nb | — | 103 | — | 132 | — |
| | APB ($mJ/m^2$) | 0Nb | 256[a], 257[f] | 160 | 213 | 471 | — |
| | | 6Nb | — | 166 | — | 388 | — |
| | CSF ($mJ/m^2$) | 0Nb | 320[a] | 212 | 309 | 327 | — |
| | | 6Nb | — | 172 | — | 190 | — |

[a]Qi et al., 2023
[b]Lu et al., 2023
[c]Seko, 2020
[d]Yoo and Fu, 1998
[e]Woodward and Rao, 2004
[f]Koizumi et al., 2006.

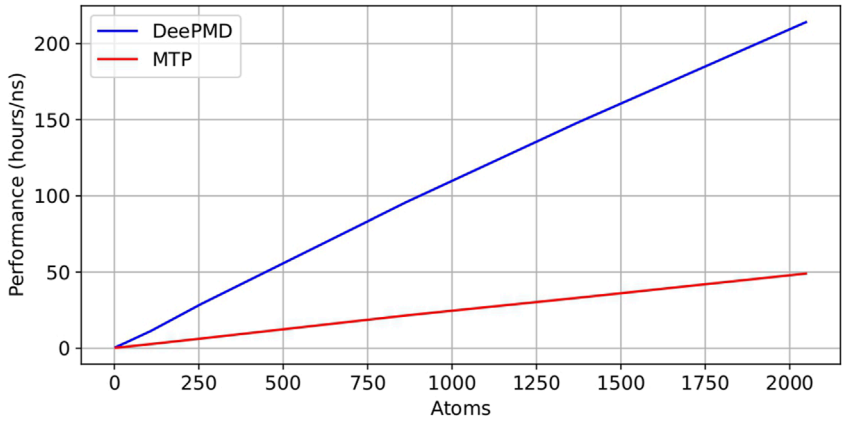


FIGURE 14
Comparison of performance (hours/ns) of DeePMD and MTP potentials in performing MD simulations.

(hours/ns) for varying numbers of atoms, specifically 4, 32, 108, 256, 864, 1,372, and 2048, in systems composed of $\gamma$-TiAl. These evaluations were conducted through short NPT simulations over a duration of 1 picosecond.

Our results demonstrate a linear correlation between computational time and atom count for both MTP and DeePMD potentials, highlighting the scalability of each potential with increasing system size. This aspect is crucial for simulations that

TABLE 6 Comparison of the timing breakdown for MPI tasks in MD simulations using DeePMD *versus* MTP potentials.

| Tasks | MTP (seconds) | DeePMD (seconds) |
|---|---|---|
| Force computation | 44.81 | 205.67 |
| Inter-processor communication | 1.15 | 4.33 |
| Output | 0.93 | 2.86 |
| Modify | 0.03 | 0.08 |
| Other | 1.41 | 2.73 |

involve large numbers of atoms. The "hours/ns" performance metric offers crucial insights into the computational demands, quantifying the time needed to complete 1 nanosecond of MD simulation. A significant efficiency disparity is evident from Figure 14, with MTP potential-based simulations exhibiting markedly superior speed compared to those employing DeePMD potential.

For a granular quantitative comparison, Table 6 details the message passing interface (MPI) task timings in an NVT simulation with 108 atoms over a span of 4 picoseconds (ps) for both potentials. Notably, MD simulations (NVT ensemble at 300 K for 4 ps on a system of 108 atoms) with DeePMD potential required 14.978 h/ns, whereas those with MTP potential required only 3.356 h/ns. This finding indicates that the MTP potential is approximately 4.5 times more efficient than the DeePMD potential. Furthermore, Table 6 delineates the time distribution across different simulation processes such as force computation, interprocessor communication, output generation, modifications via fixes, and other related tasks. These tests were carried out on a high-performance computing (HPC) cluster utilizing a single node equipped with 48 processors. This detailed breakdown unequivocally shows that simulations with the DeePMD potential consume more computational time than those with the MTP potential for identical simulation conditions.

## 4 Conclusion

In our study, we conducted a comparative analysis of the interatomic potentials for TiAlNb alloys, developed through both MTP and deep learning approaches. We introduced a comprehensive dataset for TiAlNb alloys, aimed at serving as a benchmark for studying the Nb-alloyed phases of $\alpha_2$-$Ti_3Al$ and $\gamma$-TiAl. Through our evaluation of the errors and performance metrics of these generated potentials, we concluded that MTP potentials offer a viable alternative in scenarios with limited computational resources. This is attributed to the lower computational cost of MD simulations relying on MTP, alongside its lower dataset requirements for effective training. However, it is important to note a slight compromise in accuracy when opting for MTP over DeePMD, despite the error margins remaining within acceptable bounds. MTP emerges as a preferable choice for applications where precise energy and force calculations are not paramount. Conversely, for endeavors requiring very high fidelity in energy and force predictions, and where it is possible to allocate more computational resources and training data, DeePMD stands out as the preferred choice. The entire workflow, encompassing dataset generation, method comparison, and the resulting conclusions, is comprehensively illustrated in Figure 15.

Our study analyzed material parameters like equilibrium volume, lattice constants, and elastic constants, revealing MTP's equilibrium volume predictions were closer to DFT results than DeePMD's for both $\alpha_2$-$Ti_3Al$ and $\gamma$-TiAl phases. MTP also provided more accurate lattice parameters for the $\alpha_2$-$Ti_3Al$ phase, while both methods agreed on the $\gamma$-TiAl phase. Elastic constant predictions of both deviated from DFT, but were more accurate for $\gamma$-TiAl. RDF curves from both models correlated well with DFT, especially

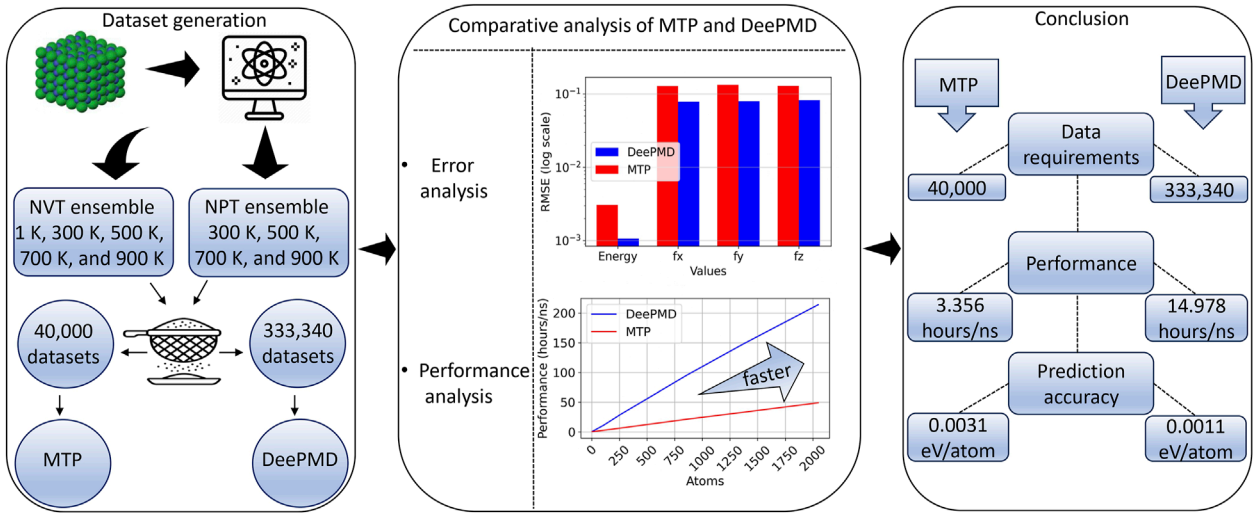


FIGURE 15
Comparison of MTP and DeePMD methods for interatomic potential generation for TiAlNb alloys.

for $\gamma$-TiAl. Finite temperature properties such as specific heat and thermal expansion coefficients were in good agreement with their corresponding DFT and experimental data. Simulations of uniaxial tension tests indicated that Nb alloying decreases the strength of TiAl-based alloys, with the exception of the results from DeePMD for $\gamma$-TiAl. Additionally, computations of stacking fault energy revealed that Nb alloying enhances the ductility of TiAl-based alloys at the expense of strength, except in simulations using DeePMD for $\gamma$-TiAl. These findings align with the outcomes of our prior work (Chandran et al., 2024). Moreover, the results for generalized stacking faults—except for the DeePMD simulations of $\gamma$-TiAl—are consistent with those reported in Dumitraschkewitz et al. (2017) for Nb-alloyed systems and in Lu et al. (2023); Qi et al. (2023) for Nb-free systems, where the sequence SISF < CSF < APB has been accurately reproduced. This succinct analysis highlights the advantages and limitations of MTP and DeePMD in simulating TiAlNb alloys, guiding researchers towards the most suitable computational strategy in view of a trade-off between accuracy and resource needs.

During the model training phase, we encountered difficulties in accurately capturing the $\alpha_2$-$Ti_3Al$ phase characteristics using both models. To address this and enhance model performance, our future work will incorporate advanced learning techniques, like active learning, into our methodology. This strategy aims to significantly improve model accuracy while reducing the reliance on extensive datasets.

## Data availability statement

The datasets presented in this study can be found in online repositories. The names of the repository/repositories and accession number(s) can be found below: https://zenodo.org/uploads/10639914.

## Author contributions

AC: Conceptualization, Data curation, Formal Analysis, Investigation, Methodology, Software, Visualization, Writing–original draft. AS: Validation, Writing–review and editing. CP: Validation, Writing–review and editing. PJ: Validation, Writing–review and editing. RA: Project administration, Supervision, Validation, Writing–review and editing. CC: Funding acquisition, Project administration, Supervision, Writing–review and editing, Validation.

## Funding

The author(s) declare that financial support was received for the research, authorship, and/or publication of this article. The authors gratefully acknowledge funding by the $I^2B$ project MetalMD at Helmholtz-Zentrum Hereon, Germany.

## Acknowledgments

During the preparation of this work the author(s) used ChatGpt (ChatGpt 4o-mini) in order to improve the language and readability of the text. After using this tool/service, the author(s) reviewed and edited the content as needed and take(s) full responsibility for the content of the publication.

## Conflict of interest

The authors declare that the research was conducted in the absence of any commercial or financial relationships that could be construed as a potential conflict of interest.

## Publisher's note



## Supplementary material

The Supplementary Material for this article can be found online at: https://www.frontiersin.org/articles/10.3389/fmats.2024.1466793/full#supplementary-material

## References

Appel, F., Paul, J. D. H., and Oehring, M. (2011). *Gamma titanium aluminide alloys: science and technology*. John Wiley and Sons.

Bartók, A. P., Kondor, R., and Csányi, G. (2013). On representing chemical environments. *Phys. Rev. B* 87, 184115. doi:10.1103/physrevb.87.184115

Becker, C. A., Tavazza, F., Trautt, Z. T., and Buarque de Macedo, R. A. (2013). Considerations for choosing and using force fields and interatomic potentials in materials science and engineering. *Curr. Opin. Solid State Mater. Sci.* 17, 277–283. doi:10.1016/j.cossms.2013.10.001

Behler, J. (2011). Neural network potential-energy surfaces in chemistry: a tool for large-scale simulations. *Phys. Chem. Chem. Phys.* 13, 17930. doi:10.1039/c1cp21668f

Behler, J., and Parrinello, M. (2007). Generalized neural-network representation of high-dimensional potential-energy surfaces. *Phys. Rev. Lett.* 98, 146401. doi:10.1103/physrevlett.98.146401

Blöchl, P. E. (1994). Projector augmented-wave method. *Phys. Rev. B* 50, 17953–17979. doi:10.1103/physrevb.50.17953

Chandran, A., Ganesan, H., and Cyron, C. J. (2024). Studying the effects of nb on high-temperature deformation in tial alloys using atomistic simulations. *Mater. and Des.* 237, 112596. doi:10.1016/j.matdes.2023.112596

Chen, C., Deng, Z., Tran, R., Tang, H., Chu, I.-H., and Ong, S. P. (2017). Accurate force field for molybdenum by machine learning large materials data. *Phys. Rev. Mater.* 1, 043603. doi:10.1103/physrevmaterials.1.043603

Cheng, L., Li, J., Xue, X., Tang, B., Kou, H., and Bouzy, E. (2016). Superplastic deformation mechanisms of high Nb containing TiAl alloy with (α2 + γ) microstructure. *Intermetallics* 75, 62–71. doi:10.1016/j.intermet.2016.06.003

Clemens, H., and Mayer, S. (2012). Design, processing, microstructure, properties, and applications of advanced intermetallic tial alloys. *Adv. Eng. Mater.* 15, 191–215. doi:10.1002/adem.201200231

Deng, Z., Chen, C., Li, X.-G., and Ong, S. P. (2019). An electrostatic spectral neighbor analysis potential for lithium nitride. *npj Comput. Mater.* 5, 75. doi:10.1038/s41524-019-0212-1

Deringer, V. L., Caro, M. A., and Csányi, G. (2019). Machine learning interatomic potentials as emerging tools for materials science. *Adv. Mater.* 31, e1902765. doi:10.1002/adma.201902765

Dragoni, D., Daff, T. D., Csányi, G., and Marzari, N. (2018). Achieving dft accuracy with a machine-learning interatomic potential: thermomechanics and defects in bcc ferromagnetic iron. *Phys. Rev. Mater.* 2, 013808. doi:10.1103/physrevmaterials.2.013808

Du, Y., Meng, Z., Yan, Q., Wang, C., Tian, Y., Duan, W., et al. (2022). Deep potential for a face-centered cubic cu system at finite temperatures. *Phys. Chem. Chem. Phys.* 24, 18361–18369. doi:10.1039/d2cp02758e

Dumitraschkewitz, P., Clemens, H., Mayer, S., and Holec, D. (2017). Impact of alloying on stacking fault energies in γ-tial. *Appl. Sci.* 7, 1193. doi:10.3390/app7111193

Farkas, D., and Jones, C. (1996). Interatomic potentials for ternary Nb -Ti -Al alloys. *Model. Simul. Mater. Sci. Eng.* 4 (1), 23. doi:10.1088/0965-0393/4/1/004

Gubaev, K., Podryabinkin, E. V., Hart, G. L., and Shapeev, A. V. (2019). Accelerating high-throughput searches for new alloys with active learning of interatomic potentials. *Comput. Mater. Sci.* 156, 148–156. doi:10.1016/j.commatsci.2018.09.031

Hale, L. M., Trautt, Z. T., and Becker, C. A. (2018). Evaluating variability with atomistic simulations: the effect of potential and calculation methodology on the modeling of lattice and elastic constants. *Model. Simul. Mater. Sci. Eng.* 26, 055003. doi:10.1088/1361-651x/aabc05

He, Y., Schwarz, R., Darling, T., Hundley, M., Whang, S., and Wang, Z. (1997). Elastic constants and thermal expansion of single crystal γ-tial from 300 to 750 k. *Mater. Sci. Eng. A* 239–240, 157–163. doi:10.1016/s0921-5093(97)00575-3

Hirel, P. (2015). Atomsk: a tool for manipulating and converting atomic data files. *Comput. Phys. Commun.* 197, 212–219. doi:10.1016/j.cpc.2015.07.012

Holec, D., Abdoshahi, N., Mayer, S., and Clemens, H. (2019). Thermal expansion and other thermodynamic properties of α2-$ti_3al$ and γ-tial intermetallic phases from first principles methods. *Materials* 12, 1292. doi:10.3390/ma12081292

Holec, D., Reddy, R. K., Klein, T., and Clemens, H. (2016). Preferential site occupancy of alloying elements in tial-based phases. *J. Appl. Phys.* 119. doi:10.1063/1.4951009

Klein, T., Clemens, H., and Mayer, S. (2016). Advancement of compositional and microstructural design of intermetallic γ-tial based alloys determined by atom probe tomography. *Materials* 9, 755. doi:10.3390/ma9090755

Koizumi, Y., Ogata, S., Minamino, Y., and Tsuji, N. (2006). Energies of conservative and non-conservative antiphase boundaries in $ti_3al$: a first principles study. *Philos. Mag.* 86, 1243–1259. doi:10.1080/14786430500380126

Kresse, G., and Furthmüller, J. (1996a). Efficiency of ab-initio total energy calculations for metals and semiconductors using a plane-wave basis set. *Comput. Mater. Sci.* 6, 15–50. doi:10.1016/0927-0256(96)00008-0

Kresse, G., and Furthmüller, J. (1996b). Efficient iterative schemes forab initiototal-energy calculations using a plane-wave basis set. *Phys. Rev. B* 54, 11169–11186. doi:10.1103/physrevb.54.11169

Li, J., Liu, Y., Liu, B., Wang, Y., Zhao, K., and He, Y. (2014). Effect of nb particles on the flow behavior of tial alloy. *Intermetallics* 46, 22–28. doi:10.1016/j.intermet.2013.10.004

Li, T., Hou, Q., Cui, J.-c., Yang, J.-h., Xu, B., Li, M., et al. (2024). Deep learning interatomic potential for thermal and defect behaviour of aluminum nitride with quantum accuracy. *Comput. Mater. Sci.* 232, 112656. doi:10.1016/j.commatsci.2023.112656

Li, X.-G., Hu, C., Chen, C., Deng, Z., Luo, J., and Ong, S. P. (2018). Quantum-accurate spectral neighbor analysis potential models for ni-mo binary alloys and fcc metals. *Phys. Rev. B* 98, 094104. doi:10.1103/physrevb.98.094104

Liu, P., Hou, B., Wang, A., Xie, J., and Wang, Z. (2022). Balancing the strength and ductility of ti2alc/tial composite with a bioinspired micro-nano laminated architecture. *Mater. and Des.* 220, 110851. doi:10.1016/j.matdes.2022.110851

Liu, Z., Lin, J., Li, S., and Chen, G. (2002). Effects of nb and al on the microstructures and mechanical properties of high nb containing tial base alloys. *Intermetallics* 10, 653–659. doi:10.1016/s0966-9795(02)00037-7

Lu, J., Wang, J., Wan, K., Chen, Y., Wang, H., and Shi, X. (2023). An accurate interatomic potential for the tialnb ternary alloy developed by deep neural network learning method. *J. Chem. Phys.* 158, 204702. doi:10.1063/5.0147720

Nguyen, N., Louis, S.-Y. V., Wei, L., Choudhary, K., Hu, M., and Hu, J. (2022). Predicting lattice vibrational frequencies using deep graph neural networks. *ACS Omega* 7, 26641–26649. doi:10.1021/acsomega.2c02765

Niu, H., Bonati, L., Piaggi, P. M., and Parrinello, M. (2020). *Ab initio* phase diagram and nucleation of gallium. *Nat. Commun.* 11, 2654. doi:10.1038/s41467-020-16372-9

Novikov, I. S., Gubaev, K., Podryabinkin, E. V., and Shapeev, A. V. (2021). The mlip package: moment tensor potentials with mpi and active learning. *Mach. Learn. Sci. Technol.* 2, 025002. doi:10.1088/2632-2153/abc9fe

Novikov, I. S., Suleimanov, Y. V., and Shapeev, A. V. (2018). Automated calculation of thermal rate coefficients using ring polymer molecular dynamics and machine-learning interatomic potentials with active learning. *Phys. Chem. Chem. Phys.* 20, 29503–29512. doi:10.1039/c8cp06037a

Novoselov, I., Yanilkin, A., Shapeev, A., and Podryabinkin, E. (2019). Moment tensor potentials as a promising tool to study diffusion processes. *Comput. Mater. Sci.* 164, 46–56. doi:10.1016/j.commatsci.2019.03.049

Ouadah, O., Merad, G., and Abdelkader, H. S. (2021). Atomistic modelling of the γ-tial/$\alpha_2$-ti3al interfacial properties affected by solutes. *Mater. Chem. Phys.* 257, 123434. doi:10.1016/j.matchemphys.2020.123434

Ouadah, O., Merad, G., Saidi, F., Mendi, S., and Dergal, M. (2020). Influence of alloying transition metals on structural, elastic, electronic and optical behaviors of γ-tial based alloys: a comparative dft study combined with data mining technique. *Mater. Chem. Phys.* 242, 122455. doi:10.1016/j.matchemphys.2019.122455

Pearson, W. (1958) "A handbook of lattice spacings and structures of metals and alloys," in *International series of monographs on metal Physics and physical metallurgy*. Pergamon. doi:10.1016/B978-1-4832-1318-7.50003-6

Perdew, J. P., Burke, K., and Ernzerhof, M. (1996). Generalized gradient approximation made simple. *Phys. Rev. Lett.* 77, 3865–3868. doi:10.1103/physrevlett.77.3865

Perdew, J. P., Burke, K., and Ernzerhof, M. (1997). Generalized gradient approximation made simple. *Phys. Rev. Lett.* 78, 1396. doi:10.1103/physrevlett.78.1396

Podryabinkin, E. V., and Shapeev, A. V. (2017). Active learning of linearly parametrized interatomic potentials. *Comput. Mater. Sci.* 140, 171–180. doi:10.1016/j.commatsci.2017.08.031

Podryabinkin, E. V., Tikhonov, E. V., Shapeev, A. V., and Oganov, A. R. (2019). Accelerating crystal structure prediction by machine-learning interatomic potentials with active learning. *Phys. Rev. B* 99, 064114. doi:10.1103/physrevb.99.064114

Qi, J., Aitken, Z. H., Pei, Q., Tan, A. M. Z., Zuo, Y., Jhon, M. H., et al. (2023). Machine learning moment tensor potential for modeling dislocation and fracture in l10–TiAl and d019–ti3Al alloys. *Phys. Rev. Mater.* 7, 103602. doi:10.1103/physrevmaterials.7.103602

Rodriguez, A., Lam, S., and Hu, M. (2021). Thermodynamic and transport properties of lif and flibe molten salts with deep learning potentials. *ACS Appl. Mater. and Interfaces* 13, 55367–55379. doi:10.1021/acsami.1c17942

Seko, A. (2020). Machine learning potentials for multicomponent systems: the ti-al binary system. *Phys. Rev. B* 102, 174104. doi:10.1103/physrevb.102.174104

Shapeev, A. V. (2016). Moment tensor potentials: a class of systematically improvable interatomic potentials. *Multiscale Model. and Simul.* 14, 1153–1173. doi:10.1137/15m1054183

Song, L., Appel, F., Wang, L., Oehring, M., Hu, X., Stark, A., et al. (2020). New insights into high-temperature deformation and phase transformation mechanisms of lamellar structures in high nb-containing tial alloys. *Acta Mater.* 186, 575–586. doi:10.1016/j.actamat.2020.01.021

Song, Y., Yang, R., Li, D., Hu, Z., and Guo, Z. (2000). A first principles study of the influence of alloying elements on tial: site preference. *Intermetallics* 8, 563–568. doi:10.1016/s0966-9795(99)00164-8

Szlachta, W. J., Bartók, A. P., and Csányi, G. (2014). Accuracy and transferability of Gaussian approximation potential models for tungsten. *Phys. Rev. B* 90, 104108. doi:10.1103/physrevb.90.104108

Tanaka, K. (1996). Single-crystal elastic constants of gamma-tial. *Philos. Mag. Lett.* 73, 71–78. doi:10.1080/095008396181019

Tanaka, K., and Koiwa, M. (1996). Single-crystal elastic constants of intermetallic compounds. *Intermetallics* 4, S29–S39. doi:10.1016/0966-9795(96)00014-3

Tanaka, K., Okamoto, K., Inui, H., Minonishi, Y., Yamaguchi, M., and Koiwa, M. (1996). Elastic constants and their temperature dependence for the intermetallic compound ti3al. *Philos. Mag. A* 73, 1475–1488. doi:10.1080/01418619608245145

Tasnádi, F., Bock, F., Tidholm, J., Shapeev, A. V., and Abrikosov, I. A. (2021). Efficient prediction of elastic properties of ti0.5al0.5n at elevated temperature using machine learning interatomic potential. *Thin Solid Films* 737, 138927. doi:10.1016/j.tsf.2021.138927

Thompson, A., Swiler, L., Trott, C., Foiles, S., and Tucker, G. (2015). Spectral neighbor analysis method for automated generation of quantum-accurate interatomic potentials. *J. Comput. Phys.* 285, 316–330. doi:10.1016/j.jcp.2014.12.018

Thompson, A. P., Aktulga, H. M., Berger, R., Bolintineanu, D. S., Brown, W. M., Crozier, P. S., et al. (2022). LAMMPS - a flexible simulation tool for particle-based materials modeling at the atomic, meso, and continuum scales. *Comput. Phys. Commun.* 271, 108171. doi:10.1016/j.cpc.2021.108171

Togo, A. (2023). First-principles phonon calculations with phonopy and phono3py. *J. Phys. Soc. Jpn.* 92. doi:10.7566/jpsj.92.012001

Togo, A., Chaput, L., Tadano, T., and Tanaka, I. (2023). Implementation strategies in phonopy and phono3py. *J. Phys. Condens. Matter* 35, 353001. doi:10.1088/1361-648x/acd831

Unke, O. T., Chmiela, S., Sauceda, H. E., Gastegger, M., Poltavsky, I., Schütt, K. T., et al. (2021). Machine learning force fields. *Chem. Rev.* 121, 10142–10186. doi:10.1021/acs.chemrev.0c01111

Unke, O. T., Koner, D., Patra, S., Käser, S., and Meuwly, M. (2020). High-dimensional potential energy surfaces for molecular simulations: from empiricism to machine learning. *Mach. Learn. Sci. Technol.* 1, 013001. doi:10.1088/2632-2153/ab5922

Wang, H., Zhang, L., Han, J., and E, W. (2018). Deepmd-kit: a deep learning package for many-body potential energy representation and molecular dynamics. *Comput. Phys. Commun.* 228, 178–184. doi:10.1016/j.cpc.2018.03.016

Wei, Y., Zhang, Y., Lu, G.-H., and Xu, H. (2012). Effects of transition metals in a binary-phase tial–ti3al alloy: from site occupancy, interfacial energetics to mechanical properties. *Intermetallics* 31, 105–113. doi:10.1016/j.intermet.2012.06.012

Woodward, C., and Rao, S. I. (2004). *Ab-initio*simulation of (*a*/2)⟨110 screw dislocations in γ-TiAl screw dislocations in γ-tial. *Philos. Mag.* 84, 401–413. doi:10.1080/14786430310001611626

Xu, T., Li, X., Wang, Y., and Tang, Z. (2023). Development of deep potentials of molten mgcl2–nacl and mgcl2–kcl salts driven by machine learning. *ACS Appl. Mater. and Interfaces*. doi:10.1021/acsami.2c19272

Yoo, M. H., and Fu, C. L. (1998). Physical constants, deformation twinning, and microcracking of titanium aluminides. *Metallurgical Mater. Trans. A* 29, 49–63. doi:10.1007/s11661-998-0158-2

Zhang, H., Lu, D., Pei, Y., Chen, T., Zou, T., Wang, T., et al. (2023). Tensile behavior, microstructural evolution, and deformation mechanisms of a high nb-tial alloy additively manufactured by electron beam melting. *Mater. and Des.* 225, 111503. doi:10.1016/j.matdes.2022.111503

Zhang, L., Han, J., Wang, H., Car, R., and E, W. (2018a). Deep potential molecular dynamics: a scalable model with the accuracy of quantum mechanics. *Phys. Rev. Lett.* 120, 143001. doi:10.1103/physrevlett.120.143001

Zhang, L., Han, J., Wang, H., Saidi, W. A., Car, R., and Weinan, E. (2018b). "End-to-end symmetry preserving inter-atomic potential energy model for finite and extended systems," in *Neural information processing systems*.

Zhang, S., Zhang, C., Du, Z., Hou, Z., Lin, P., Kong, F., et al. (2016). Deformation behavior of high Nb containing TiAl based alloy in α + γ two phase field region. *Mater. and Des.* 90, 225–229. doi:10.1016/j.matdes.2015.10.080

Zhao, Z., Guo, W., and Zhang, Z. (2024). A general-purpose neural network potential for ti-al-nb alloys towards large-scale molecular dynamics with *ab initio* accuracy. doi:10.48550/ARXIV.2403.09529

Zuo, Y., Chen, C., Li, X., Deng, Z., Chen, Y., Behler, J., et al. (2020). Performance and cost assessment of machine learning interatomic potentials. *J. Phys. Chem. A* 124, 731–745. doi:10.1021/acs.jpca.9b08723